ADVANCING EARTH AND SPACE SCIENCES

AGU Advances

RESEARCH ARTICLE

10.1029/2024AV001549

High-Speed Electron Flows in the Earth Magnetotail

Huijie Liu[1,2], Wenya Li[1], Binbin Tang[1], Cecilia Norgren[3], Kaijun Liu[4], Yuri V. Khotyaintsev[3], Daniel Graham[3], Tongkuai Li[1,2], Chongle Zhang[1,2], Andris Vaivads[5,6], Shan Wang[7], Jiansen He[7], Xiaocheng Guo[1], James L. Burch[8], Per-Arne Lindqvist[9], Robert Ergun[10], Daniel Gershman[11,12], Benoit Lavraud[13,14], Christopher Russell[15], Quanming Lu[16,17,18], and Chi Wang[1,2]

[1]State Key Laboratory of Space Weather, National Space Science Center, Chinese Academy of Sciences, Beijing, China, [2]College of Earth and Planetary Sciences, University of Chinese Academy of Sciences, Beijing, China, [3]Swedish Institute of Space Physics, Uppsala, Sweden, [4]Department of Earth and Space Sciences, Southern University of Science and Technology, Shenzhen, China, [5]KTH Royal Institute of Technology, Stockholm, Sweden, [6]Ventspils University of Applied Sciences, Ventspils, Latvia, [7]School of Space and Earth Sciences, Peking University, Beijing, China, [8]Southwest Research Institute, San Antonio, TX, USA, [9]Department of Space and Plasma Physics, KTH Royal Institute of Technology, Stockholm, Sweden, [10]Department of Astrophysical and Planetary Sciences, University of Colorado Boulder, Boulder, CO, USA, [11]NASA Goddard Space Flight Center, Greenbelt, MD, USA, [12]Department of Astronomy, University of Maryland, College Park, MD, USA, [13]Institut de Recherche en Astrophysique et Planétologie, Université de Toulouse, CNRS, UPS, CNES, Toulouse, France, [14]Laboratoire d'Astrophysique de Bordeaux, University Bordeaux, CNRS, Pessac, France, [15]Department of Earth and Space Sciences, University of California, Los Angeles, CA, USA, [16]CAS Key Laboratory of Geospace Environment, School of Earth and Space Sciences, University of Science and Technology of China, Hefei, China, [17]Deep Space Exploration Laboratory, CAS Center for Excellence in Comparative Planetology, Hefei, China, [18]Collaborative Innovation Center of Astronautical Science and Technology, Harbin, China

Peer Review The peer review history for this article is available as a PDF in the Supporting Information.

Key Points:

- Using MMS partial moments data, 642 high-speed electron flows are identified from 2017 to 2021
- High-speed electron flows are widely distributed in the Earth magnetotail and exhibit dawn-dusk asymmetry distribution
- The high-speed electron flows exhibit distinct features in different regions and most of them are associated with magnetic reconnection

Supporting Information:

Supporting Information may be found in the online version of this article.

Correspondence to:

W. Li and B. Tang,
wyli@spaceweather.ac.cn;
bbtang@spaceweather.ac.cn

Citation:

Liu, H., Li, W., Tang, B., Norgren, C., Liu, K., Khotyaintsev, Y. V., et al. (2025). High-speed electron flows in the Earth magnetotail. *AGU Advances*, *6*, e2024AV001549. https://doi.org/10.1029/2024AV001549

Received 15 OCT 2024
Accepted 26 FEB 2025

Author Contributions:

Conceptualization: Huijie Liu, Wenya Li
Data curation: Huijie Liu
Formal analysis: Huijie Liu, Wenya Li, Binbin Tang, Cecilia Norgren, Kaijun Liu, Yuri V. Khotyaintsev, Daniel Graham, Tongkuai Li, Chongle Zhang, Shan Wang, Xiaocheng Guo, Chi Wang
Investigation: Huijie Liu, Binbin Tang
Methodology: Huijie Liu, Wenya Li, Binbin Tang, Cecilia Norgren, Yuri V. Khotyaintsev, Daniel Graham
Resources: Huijie Liu
Software: Huijie Liu, Wenya Li

Abstract High-speed electron flows (HSEFs) play a crucial role in the energy dissipation and conversion processes within the terrestrial magnetosphere and can drive various types of plasma waves and instabilities, affecting the electron-scale dynamics. The existence, spatial distribution, and general properties of HSEFs in the Earth magnetotail are still unknown. In this study, we conduct a comprehensive survey of HSEFs in the Earth magnetotail, utilizing NASA's Magnetospheric Multiscale (MMS) mission observations from 2017 to 2021. A total of 642 events characterized by electron bulk speeds exceeding 5,000 km/s are identified. The main statistical properties are: (a) The duration of almost all HSEFs are less than 4 s, and the average duration is 0.74 s. (b) HSEFs exhibit a strong dawn-dusk (30%–70%) asymmetry. (c) 39.6%, 29.0%, and 31.4% of the events are located in the plasma sheet, plasma sheet boundary layer (PSBL), and lobe region, respectively. (d) In the plasma sheet, HSEFs have arbitrary moving directions regarding the ambient magnetic field, and the events near the neutral line predominantly move along the same direction as the ion outflows, indicating outflow electrons generated by magnetic reconnection. (e) HSEFs in the PSBL and lobe mainly move along the ambient magnetic field, and 70% of HSEFs in the PSBL exhibit features of reconnection inflow. The HSEFs in lobe regions may locate near the reconnection electron edges. Our study reveals that the HSEFs in magnetotail are closely associated with magnetic reconnection, and the statistical results deepen the understanding of HSEF fundamental properties in collisionless plasma.

Plain Language Summary Super-Alfvénic high-speed electron flows carry intense current, which play a significant role in the energy dissipation and conversion process in space, solar, and astrophysical plasma environment. Simulation studies have verified their acceleration mechanisms, and the most concerned is magnetic reconnection. Due to their small scale, in situ observations of electron-scale dynamics are lacking, especially in the Earth magnetotail with rarefied plasma. NASA lunched MMS, providing abundant high-resolution electron observations, and have reported several high-speed electron flows near the magnetotail reconnection up to date. The existence, spatial distribution, and general properties of HSEFs in the Earth magnetotail are still unknown. Our investigation presents a comprehensive survey of high-speed electron flows and analyses their relation with magnetic reconnection.

1. Introduction

The super-Alfvénic fast flows as the medium for the transport of energy and matter are widely distributed in space, solar, and astrophysical plasma environment (Lazarian & Opher, 2009; Lin et al., 2003; Lin & Hudson, 1971). It is

Supervision: Wenya Li, Binbin Tang, Cecilia Norgren, Kaijun Liu
Validation: Huijie Liu, Wenya Li, Binbin Tang
Visualization: Huijie Liu, Wenya Li, Binbin Tang, Cecilia Norgren
Writing – original draft: Huijie Liu
Writing – review & editing: Huijie Liu, Wenya Li, Binbin Tang, Cecilia Norgren, Kaijun Liu, Yuri V. Khotyaintsev, Daniel Graham, Tongkuai Li, Chongle Zhang, Andris Vaivads, Shan Wang, Jiansen He, James L. Burch, Per-Arne Lindqvist, Robert Ergun, Daniel Gershman, Benoit Lavraud, Christopher Russell, Quanming Lu

well established that magnetic reconnection is an important mechanism that generates the super-Alfvénic fast plasma flows by converting the magnetic energy to plasma energy. The Earth magnetotail is a key region of magnetosphere convection and explosive space activities and has attracted extensive studies. Commonly, the magnetotail is separated into four regions, including the plasma sheet (PS), plasma sheet boundary layer (PSBL), lobe, and boundary layer at the magnetopause (Frank, 1985). The plasma sheet is a large plasma reservoir, where explosive magnetic reconnection and various types of plasma instabilities are frequently triggered (Frank, 1985). Due to reconnection and instabilities, a large amount of plasmas and magnetic fluxes can be released and enter the near-Earth magnetosphere. Dramatic space weather activities can be triggered, such as substorm and magnetic storm, that can greatly endanger space-based facilities (Angelopoulos et al., 2008; Baker et al., 1996; Baumjohann et al., 1999). The main carrier of the magnetic fluxes is the high-speed ion flow, which is widely known as bursty bulk flow (BBF, Angelopoulos et al., 1997; Nakamura et al., 2002; Kaufmann et al., 2005). Extensive studies using in situ observations (Baumjohann et al., 1989; Cao et al., 2006; Nagai et al., 1998) and numerical simulations (C. X. Chen & Wolf, 1993; Shay et al., 2003) have provided a comprehensive understanding of the high-speed ion flows, including their generation mechanism, spatiotemporal scales, plasma parameters, and accompanying plasma waves. Most of time, high-speed ion flows also exist inside the plasma sheet boundary layer, in the form of fast field-aligned ion beams (Baumjohann et al., 1989; Birn et al., 2015; Onsager et al., 1991). The regions outside of PSBL, known as northern and southern lobes, are mostly stagnant and tenuous (Gosling et al., 1985; Haaland et al., 2008; Svenes et al., 2008). The field-aligned current, predominantly carried by electrons, couples the dynamics between magnetosphere and ionosphere, and the super Alfvénic electron flows may directly link the exploring site in the magnetotail and the disturbed ionospheric regions (Milan et al., 2017).

Due to the small electron mass, the electron dynamics, especially the acceleration process, exhibit different properties in the magnetotail from the ion dynamics. Oieroset et al. (2001) reported a serendipitous encounter of an electron diffusion region of on-going reconnection in the distant magnetotail by the Wind spacecraft and showed electron beams with energies below 300 eV, contributing to the Hall current. Nagai et al. (2013) reported more detailed differences in the dynamics of electrons and ions in the ion-electron decoupling region using Geotail data, including velocity, energy spectra, and distribution functions. Besides the observational studies, numerical simulations focused more on the acceleration of the non-thermal electrons in the reconnection diffusion region (Drake et al., 2003; Fu et al., 2006; Hoshino et al., 2001; C. Huang et al., 2010; Pritchett, 2008), separatrices (Cattell et al., 2005; Q. Lu et al., 2010; R. Wang et al., 2010), merging magnetic islands (Pritchett, 2008), and ion outflows (Imada et al., 2007). In addition, when there is a guide field, the acceleration efficiency of electrons come from the region outside of the negative separatrices is more enhanced than in the anti-parallel reconnection due to the gyration motion (Fu et al., 2006; C. Huang et al., 2010). The properties and acceleration mechanism of electron bulk motion remain unclear.

To resolve the electron-scale processes in space, NASA launched the Magnetospheric Multiscale (MMS) mission in 2015. Four identical MMS spacecraft fly in an adjustable pyramid-like formation, and the average separation between the four satellites changes from 7 to 160 km (Burch, Moore, et al., 2016). Each spacecraft has a suite of high-resolution instruments, among which the Fast Plasma Investigation (FPI) provides three-dimensional (3D) electron velocity distribution functions (eVDFs) with a resolution of 30 ms (Pollock et al., 2016). The early phase (2015–2016) of MMS focused on the electron-scale processes at the dayside magnetopause. Burch, Torbert, et al. (2016) reported an MMS encounter of a magnetopause electron diffusion region on 2015 October 16, where the observed super-Alfvénic (∼1,100 km/s) electron flow carries the electron-scale intense current and contributes to the energy conversion and dissipation. Until now, many event studies have investigated the properties of high-speed electron flows in EDRs under various boundary conditions (Graham et al., 2019; Y. V. Khotyaintsev et al., 2016; W. Y. Li et al., 2020; Phan et al., 2016; Webster et al., 2018). Recently, Man et al. (2021) presented a statistical study of the intense currents in the magnetopause boundary layer and revealed the features of energy dissipation associated with the fast electron flows.

In the magnetotail, the magnetic field magnitude (∼10 nT) in the plasma sheet is roughly 2–3 times lower than that at the magnetopause, while the plasma density (0.05–0.2 cm^{-3}) is approximately two orders of magnitude lower than that at the magnetopause, indicating that the characteristic velocities, for example, ion and electron Alfvén velocities, are approximately five times larger than those at the magnetopause. Several studies have reported high-speed electron flows in the vicinity of reconnection X lines (L. J. Chen et al., 2019; Ergun et al., 2018; W. Y. Li et al., 2021; Tang et al., 2022; Torbert et al., 2018; S. Wang et al., 2022; Zhou et al., 2019), with bulk speeds ranging from 5,000 km/s to 1.8×10^4 km/s. Their bulk velocities are predominantly from the meandering motion along the reconnection out-of-plane direction and outflow motion along the reconnecting magnetic field direction. The properties of those high-speed electron flows are crucial for understanding the dynamics and instabilities of the thin current sheet at the X-line and the partition and dissipation of the electromagnetic energy. Norgren et al. (2020) showed that high-speed electron flows are parallel to the ambient magnetic field and move toward the X-line in the reconnection separatrix. Those flows drive large-amplitude electrostatic solitary waves, which in turn thermalize the high-speed electrons. Those event studies presented primary understanding of the high-speed electron flows in the magnetotail, and the statistical studies are still lacking.

Using MMS observations in the magnetotail from May to August in 2017, S. Y. Huang et al. (2020) performed a statistical study on the electron jets with number densities larger than 0.1 cm^{-3}, whose speeds are mostly in the range of 500–2,000 km/s. Those electron jets exhibit nearly symmetric distribution along the dawn-dusk direction, and their distribution regions and structures, including current sheets, dipolarization fronts (DFs), magnetotail holes, PSBL, and flux ropes, were also analyzed. L. Wang et al. (2022) studied the DFs in the magnetotail statistically and found that $\sim$1 keV electrons are the main carriers of the Hall current at DFs. W. Ma et al. (2022) conducted a statistical study on the electron acceleration mechanisms in the magnetotail and found that betatron acceleration and first-order Fermi acceleration mainly occur near the neutral sheet, while parallel electric field acceleration is not only observed near the neutral sheet but also in regions far from the neutral sheet, such as reconnection separatrices. Using a newly developed algorithm, Rogers et al. (2023) identified 12 ion diffusion regions (IDRs) in the magnetotail, and 11 of them are located in the dusk magnetotail, consistent with previous studies on the dawn-dusk asymmetry of BBFs (Raj et al., 2002), flux ropes (Imber et al., 2011), current sheets (S. Lu et al., 2016), and DFs (Xiao et al., 2017). Hubbert et al. (2022) found that the electron-only reconnetion is the transition phase from quiet current sheet to traditional ion-coupled reconnection, based on a statistical study on the MMS current-sheet observations from 2017 to 2020. All those previous statistical studies illustrate that widely distributed fast electron flows play an important role in the kinetic processes and dynamic structures in the terrestrial magnetotail.

However, the high-speed electron flows in the magnetotail lack a comprehensive survey, and their overall distribution and properties are still unclear. Here, we perform a systematic survey of the high-speed electron flows in the Earth magnetotail and investigate their statistical properties. We compute the partial moments of ions and electrons from the three-dimensional VDFs, and the method as well as the event selection criteria are presented in Section 2. In Section 3, we show three high-speed electron flow examples in an EDR, the PSBL, and the lobe region, respectively. Section 4 presents their statistical results and the conclusions are in Section 5.

2. MMS and Event Selection Criteria

2.1. Magnetospheric Multiscale Mission

NASA launched the Magnetospheric Multiscale mission on 2015 March 12, which consists of four identical satellites flying in a tetrahedron configuration in space to resolve the electron-scale processes in the Earth's magnetosphere (Burch, Moore, et al., 2016). Each spacecraft carries a suite of high-resolution in situ instruments. The plasma data are provided by the Fast Plasma Investigation, which can provide the burst-mode electron and ion measurements with time resolutions of 30 and 150 ms, respectively (Pollock et al., 2016). We also use the ion data from the Fly's Eye Energetic Particle Sensor (FEEPS, Blake et al., 2016; Mauk et al., 2016) and the mass-resolved instrument Hot Plasma Composition Analyzer (HPCA, Young et al., 2016). The electric field data are measured by the Spin-plane Double Probe (SDP, Lindqvist et al., 2016) and the Axial Double Probe (ADP, Ergun et al., 2016) instruments with resolution from DC to $\sim$100 kHz. The magnetic field data are measured by the Fluxgate Magnetometer (FGM, Russell et al., 2016) with 128 samples/s. So far, MMS have been in orbit for 9 years and collected a large amount of high-quality data.

The early operation phase (2015–2016) of MMS, with an apogee of 12 R_E (Earth radius), focused on the processes along the dayside magnetopause boundary. Then, the apogee increased to 25 R_E in 2017 and 28 R_E in 2019, and MMS were capable of detecting the processes in and near the plasma sheet in the middle magnetotail. Since May in 2017, MMS began to observe the magnetotail, and the orbit covered the magnetotail roughly from May to September of each year from 2017 to 2021, providing an opportunity for systematic investigation on the high-speed electron flows in the Earth magnetotail. The ion sensors and electric and magnetic field instruments

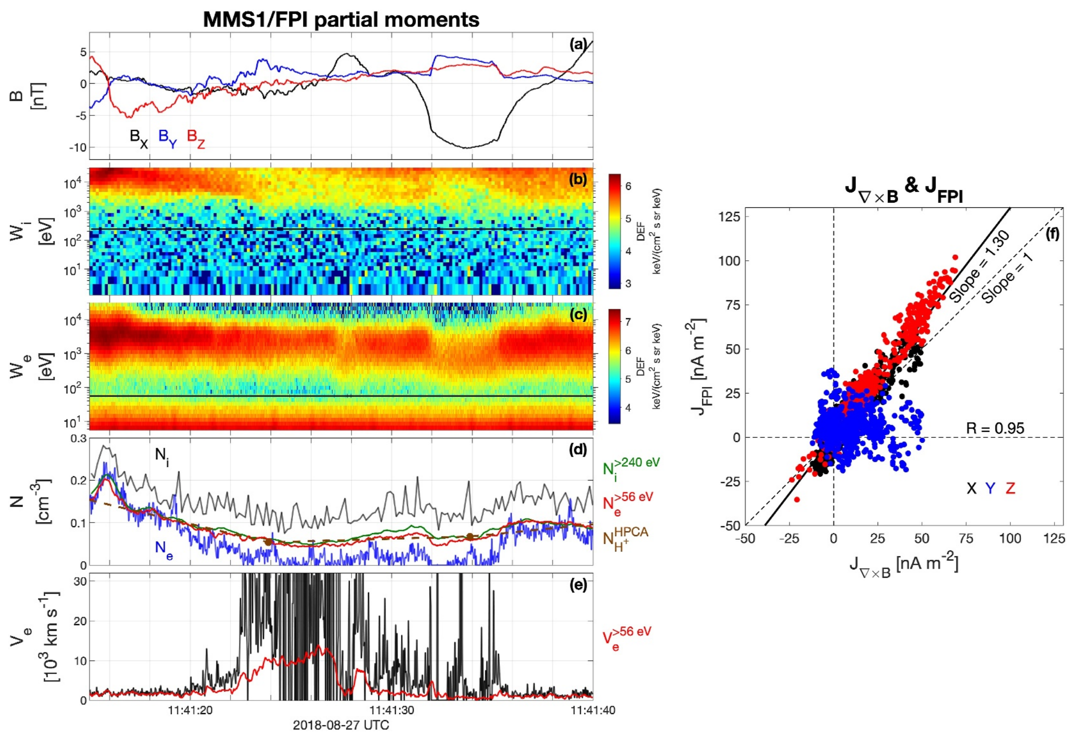

Figure 1. An example of the FPI partial moments. (a) Magnetic field $\boldsymbol{B}$ in Geocentric Solar Ecliptic (GSE) coordinate system. (b) Ion and (c) electron omni-directional differential energy fluxes. The black horizontal lines in panels (b) and (c) represent the start energies ($W_i = 240$ eV and $W_e = 56$ eV) of the partial-moment calculation. (d) Number density N. The black (N_i) and blue (N_e) curves are from the FPI zero-order moment data (dis-moms and des-moms), and the green $\left(N_i^{>240\ \mathrm{eV}}\right)$ and red $\left(N_e^{>56\ \mathrm{eV}}\right)$ curves are from the partial-moment calculation. The brown dashed curve is the hydrogen ion number density $\left(N_{H^+}^{\mathrm{HPCA}}\right)$. (e) Electron bulk speed V_e. The black curve is from the FPI first-order moment data, and the red $\left(V_e^{>56\ \mathrm{eV}}\right)$ curve is from the partial moments. (f) Comparison between the FPI current density $\boldsymbol{J}_{\mathrm{FPI}} = q_e N_e^{>56\ \mathrm{eV}}(\boldsymbol{V}_i^{>240\ \mathrm{eV}}\text{-}\boldsymbol{V}_e^{>56\ \mathrm{eV}})$ and $\boldsymbol{J}_{\nabla\times B} = \nabla \times \boldsymbol{B}/\mu_0$ from the four-spacecraft curlometer method. Here, $\boldsymbol{J}_{\mathrm{FPI}}$ represents the average results of the available spacecraft. $\boldsymbol{J}_{\mathrm{FPI}}$ and $\boldsymbol{J}_{\nabla\times B}$ have a high correlation coefficient ($R = 0.95$), and their linear fitting slope is 1.30 for this case.

onboard the four spacecraft operated well in the investigated years (2017–2021). Two quadrants of the MMS4 electron spectrometer have been turned off since 2018 July 15 due to an anomaly, and the MMS4 burst-mode electron moments data have been unavailable since then.

2.2. FPI Partial Moments

The plasma in the terrestrial magnetotail are tenuous, with number densities on the order of 0.1 cm^{-3}. The detection from an electrostatic analyzer in the magnetotail can be commonly affected by the solar extreme ultraviolet (EUV) emission and high-energy particles (Gershman et al., 2019). Figures 1b and 1c show an example of the FPI ion and electron energy spectrograms observed in the magnetotail on 2018 August 27, near the MMS apogee. Their zero-order moments based on an integral over all energy channels (6.5 eV–27.5 keV) are presented by the black and blue curves in Figure 1d, respectively, and one can easily notice the significant discrepancy between them. For ion detection, the high-energy particles can penetrate into the instrument and produce nearly constant background in all energy segments (Gershman et al., 2019), as one can see from the bluish colors in the ion energy spectrogram (Figure 1b). Thus, N_i from the all energy integral is overestimated. One simple way to reduce this effect by the penetrating radiation is to start the integral from a relatively high energy. For the analysis in this study, the start energy is chosen to be 240 eV (black horizontal line in Figure 1b), as have been suggested by the FPI team (Gershman et al., 2017). For the example case, the ion partial number density $\left(N_i^{>240\ \mathrm{eV}}\right)$ is presented by the green curve in Figure 1d.

For electron detection, the secondary electrons are produced when solar EUV photons hit the spacecraft and the instruments. There are two populations of photoelectrons measured at low energies by the FPI dual electron spectrometers (DES). One is the spacecraft photoelectrons measured at energies below the spacecraft potential, which is usually positive in the magnetotail. The other one is the secondary electrons produced inside the DES sensors, which are independent of the ambient plasma conditions and spacecraft potential (Gershman et al., 2017). For the example shown in Figure 1c, the spacecraft potential is approximately 4.3 V, below the lowest energy (6.5 eV) of the FPI DES sensors, while there exist secondary electrons with significant energy fluxes from the lowest energy channel up to ∼30 eV. The FPI algorithm for producing the electron moments adopts a model distribution function to remove those secondary electrons (Gershman et al., 2017), which may over-subtract the signal of ambient electrons. This can cause unphysical moments, including zero number density (N_e, Figure 1d) and extremely large electron bulk speed (black curve in Figure 1e). The energies of those secondary electron are significantly lower than 50 eV, while the typical electron energy in the magnetotail is generally above 50 eV (Vo et al., 2023). Here, we use 56 eV as the start integral energy (black horizontal line in Figure 1c) to remove the secondary electrons, and apply it throughout the text. For the example case, the electron partial number density ${N_e}^{>56\ \mathrm{eV}}$ is presented by the red curve in Figure 1d, and the partial bulk speed ${V_e}^{>56\ \mathrm{eV}}$ is shown by the red curve in Figure 1e. These electron partial moments are five-point averaged to further reduce statistical errors by low counts.

As a verification, we overplot the 10-s resolution proton number density $N_{H^+}^{\mathrm{HPCA}}$ from HPCA in Figure 1d. One can see that the ion $\left({N_i}^{>240\ \mathrm{eV}}\right)$ and electron $\left({N_e}^{>56\ \mathrm{eV}}\right)$ partial number densities and $N_{H^+}^{\mathrm{HPCA}}$ match up with each other. Furthermore, we compare the current density from the partial moments $\boldsymbol{J}_{\mathrm{FPI}} = q_e {N_e}^{>56\ \mathrm{eV}}\ (\boldsymbol{V}_i^{>240\ \mathrm{eV}}\text{-}\boldsymbol{V}_e^{>56\ \mathrm{eV}})$ with the current density from the Ampere's law $\boldsymbol{J}_{\nabla\times B} = \nabla \times \boldsymbol{B}/\mu_0$ (μ_0 is permeability in vacuum) using the four-spacecraft curlometer method (Paschmann & Daly, 1998). Figure 1f shows the comparison. $\boldsymbol{J}_{\mathrm{FPI}}$ and $\boldsymbol{J}_{\nabla\times B}$ have a good correlation coefficient ($R = 0.95$), and their linear slope is 1.30, denoting reliable calculation of the FPI partial moments. We use 240 and 56 eV as the start integral energy of ion and electron partial moments in this study, and their corresponding notations are simplified as N_i, N_e, $\boldsymbol{V}_i$, and $\boldsymbol{V}_e$ in the following sections.

2.3. Event Selection Criteria

In this study, we focus on the magnetotail events with extremely high-speed electron flows with bulk speed over 5,000 km/s, which is super-Alfvénic and much larger than the moment noise of FPI in the magnetotail. As shown in Figure 2a, MMS observe three high-speed electron flows with V_e>5,000 km/s in the event of Figure 1. The maximum peak speeds (highlighted by filled circles) are captured by MMS1, MMS2 and MMS3, respectively, and the shaded intervals by the corresponding colors denote the full widths at half peaks (T_{HP}), which are derived from the satellite who observed the maximum peak speeds. Using this speed criterion, we identify 869 events in the MMS magnetotail database between 2017 and 2021. The events in the magnetopause boundary layer are not included in this event list. The scatter plot and one-dimensional (1D) histograms of R and the slopes of $\boldsymbol{J}_{\nabla\times B}$ and $\boldsymbol{J}_{\mathrm{FPI}}$ are presented in Figures 2b–2d. Here, R and the slopes are computed within T_{HP} for each event. In Figure 2c, most of events have good correlation coefficients between $\boldsymbol{J}_{\nabla\times B}$ and $\boldsymbol{J}_{\mathrm{FPI}}$, and we select the events with R larger than 0.7 to further increase the reliability. In Figure 2d, most of the events have $\boldsymbol{J}_{\mathrm{FPI}}$ larger than $\boldsymbol{J}_{\nabla\times B}$, and their linear slopes have the highest count at 1.2. As the example shown in Figures 1f and 2a, one or more MMS spacecraft may capture localized electron-scale processes with intense current densities, resulting in relatively large average $\boldsymbol{J}_{\mathrm{FPI}}$, while $\boldsymbol{J}_{\nabla\times B}$ represents the average current density at the barycenter of the tetrahedron. Also, only three or even less spacecraft are available from July 2018, and those observations when intense current sheets are encountered give even larger $\boldsymbol{J}_{\mathrm{FPI}}$ than $\boldsymbol{J}_{\nabla\times B}$. In our analysis, we choose event slopes with counts roughly over 30% of the peak count, which gives the slopes range between 0.8 and 1.5, denoted by the blue dashed lines in Figure 2d and the blue bar in Figure 2b. Finally, 642 high-speed electron flows are selected from the investigated database.

3. Examples of High-Speed Electron Flows

Previous studies have reported high-speed electron flows in EDRs (Ergun et al., 2018; W. Y. Li et al., 2021; Tang et al., 2022; Torbert et al., 2018; Zhou et al., 2019) and reconnection separatrix (Norgren et al., 2020). The high-speed electron flows carry intense electron-scale current densities in those regions and are associated with various types of plasma waves. In our event list, the high-speed electron flows are widely observed in different regions

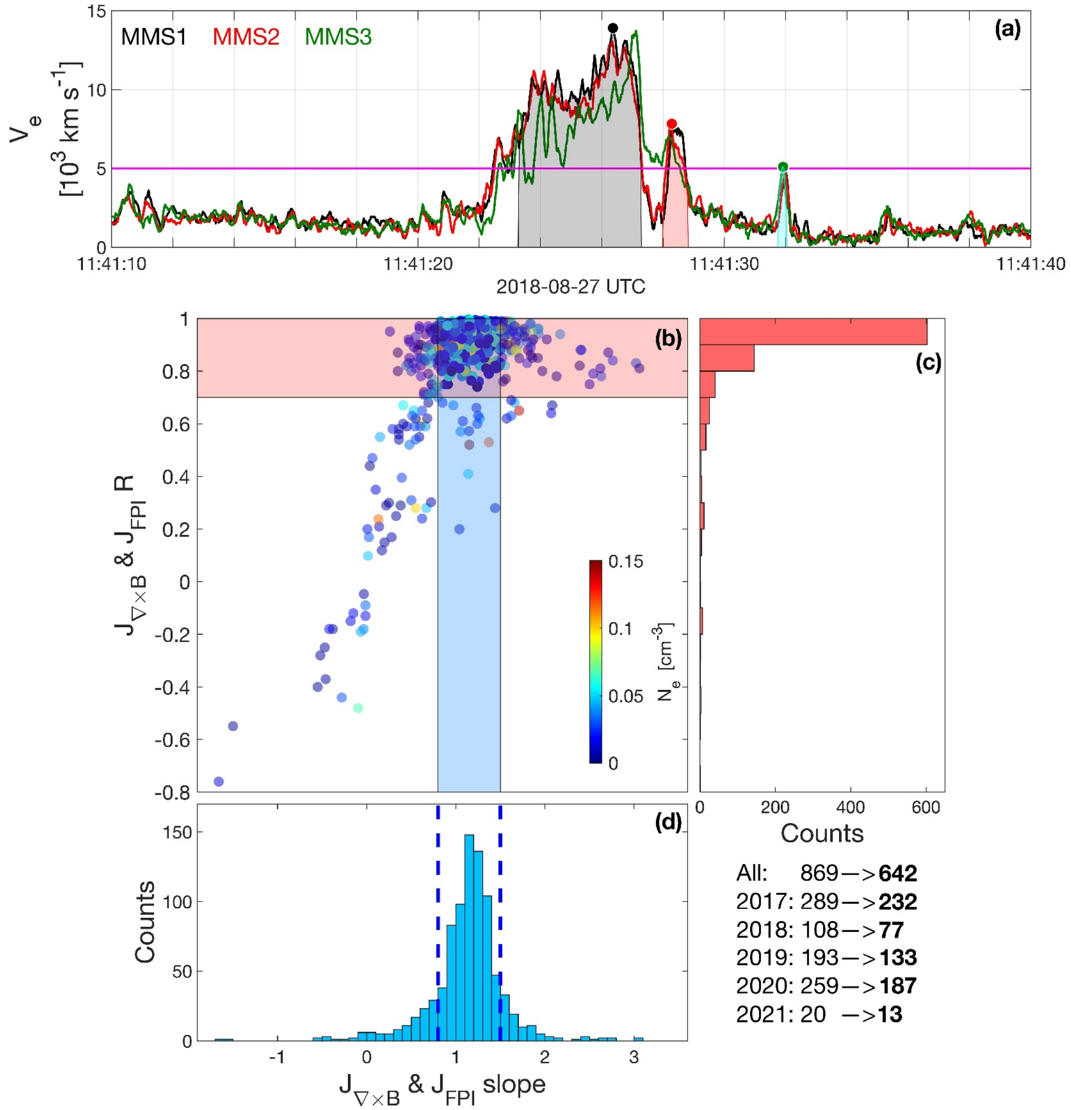

Figure 2. Selection criteria of the high-speed electron flows. (a) Electron bulk speed V_e of the example event in Figure 1. The three filled circles denote the V_e peaks of three high-speed electron flows with speeds over 5,000 km/s (denoted by the horizontal magenta line), which are observed by MMS1, MMS2 and MMS3, respectively. The three color-shaded bars show the full widths at half peaks. (b) Scatter plot of the current-density linear slopes and correlation coefficients (R) of the 869 selected events with V_e>5,000 km/s from the MMS magnetotail observations in 2017–2021. The events are colored by N_e. Histograms of panel (c) R and (d) linear slopes. In panel (b), the blue bar denotes the slope range from 0.8 to 1.5 (also represented by the two blue dashed lines in panel (d)), and the red bar denotes R larger than 0.7. 642 events are finally selected based on those two criteria. The numbers in the bottom-right corner show the event counts before and after the slope and R constraints.

with varying magnetic-field conditions, including EDR candidates with weak magnetic field, the plasma sheet boundary layer with energetic (~keV) ions and large-amplitude $\boldsymbol{B}$, and lobe region with negligible energetic ions and low plasma beta. In this section, we will show three examples of high-speed electron flows observed in those regions.

3.1. Example 1: High-Speed Electron Flow in an EDR

Figure 3 presents an MMS2 overview of magnetotail neutral sheet observations starting from 23:00:42.5 UT on 2020 August 26. In this event, the four MMS spacecraft were located at [−26.4, 8.5, 3.4] R_E in GSE coordinates and were in a tetrahedron formation with an average separation of 37 km. We perform a minimum variance analysis (MVA, Paschmann & Daly, 1998) on the magnetic field data to establish a local coordinate system,

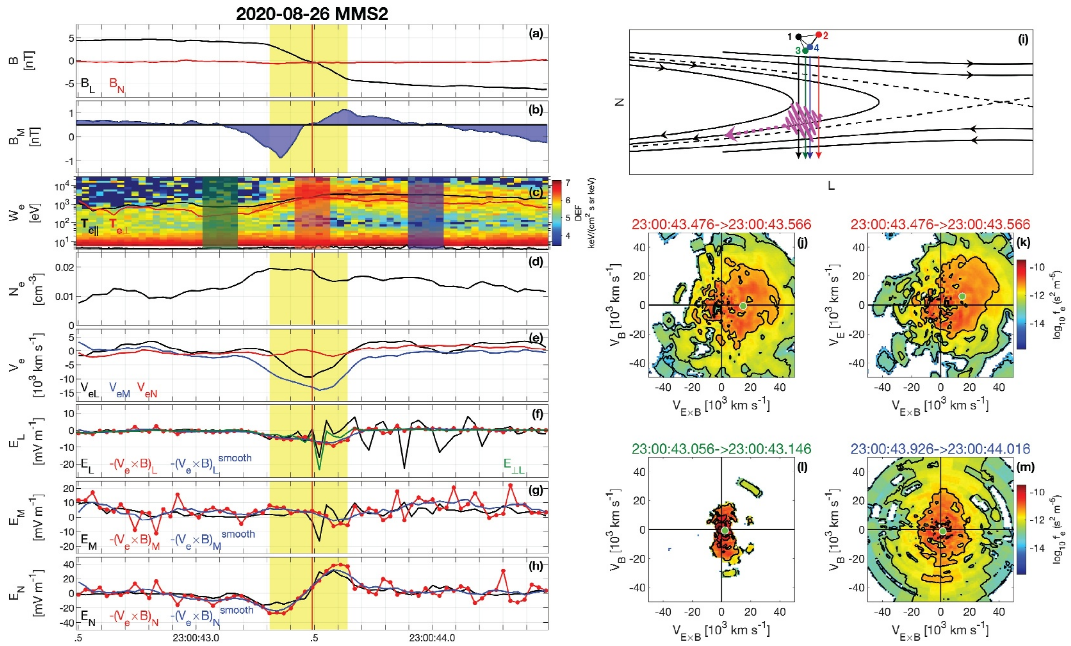

Figure 3. An HSEF example associated with a magnetotail EDR observed by MMS2 on 2020 August 26. (a) B_L (black) and B_N (red). (b) B_M. The black line in panel (b) represents the guide field ($B_g \approx 0.49$ nT). (c) Electron omni-directional differential energy flux with electron parallel (black, $T_{e\parallel}$) and perpendicular (red, $T_{e\perp}$) temperatures. The black curve in the bottom part of panel (c) is the spacecraft potential. (d) N_e. (e) $\boldsymbol{V}_e$ in LMN. (f) **L**, (g) **M**, and (h) **N** components of the measured electric field $\boldsymbol{E}$ (black), unsmoothed (red), and five-point smoothed (blue) electron convection electric field $-\boldsymbol{V}_e \times \boldsymbol{B}$. The green curve in panel (f) represents the **L** component of perpendicular electric field $E_{\perp L}$. Here, $\boldsymbol{E}$ are down sampled to 30-ms resolution. (i) Sketch of the MMS crossing through the EDR. (j) and (k) Two-dimensional (2D) reduced electron velocity distribution functions (eVDFs) in the $\boldsymbol{V}_{E\times B}$-$\boldsymbol{V}_B$ and $\boldsymbol{V}_{E\times B}$-$\boldsymbol{V}_E$ planes at the time interval indicated by the red bar in panels (c). (l) and (m) 2D reduced eVDFs in the northern (+**N**, green bar in panel (c)) and southern (−**N**, blue bar in panel (c)) inflow regions. The green filled circle in each panel denotes the projected electron bulk velocity.

which yields **L** = [0.97, −0.26, 0.03], **M** = [0.23, 0.79, −0.57], and **N** = [0.12, 0.56, 0.82] in GSE. The vectors in Figure 3 are all presented in LMN coordinates.

In this event, MMS2 is initially located on the northern side of the current sheet, characterized by a positive B_L of ~4.45 nT (Figure 3a). The plasma number density is approximately 0.01 cm^{-3} (Figure 3d), and the electron scalar temperature is 431 eV, with a temperature anisotropy ($T_{e\parallel} > T_{e\perp}$). At 23:00:43.47 UT, B_L reverses sign, indicating that MMS2 crosses the neutral sheet in the magnetotail. At the same time, a significant increase in N_e (0.02 cm^{-3}, Figure 3d) is observed, and the corresponding electron inertial length (d_e) is 37.5 km. Subsequently, MMS2 enters the southern side of the current sheet, with a B_L of −5.67 nT (Figure 3a), a decreased number density of 0.016 cm^{-3} (Figure 3d), and an electron temperature of 2.1 keV. Around the B_L reversal, a high-speed electron flow is observed, with the peak speed of 1.6×10^4 km/s captured by MMS2 (Figure 3e). Its duration (T_{HP}) is 0.33 s, corresponding to the yellow shaded region in Figures 3a–3h. Within T_{HP}, MMS2 observes a large $V_{eM} \sim -1.3 \times 10^4$ km/s (Figure 3e), carrying an intense current $J_M \sim 40.1$ nA/m^2 at the neutral sheet. Moreover, MMS1-3 observe an enhanced tailward electron flow in this event, with the peak speed reaching $V_{eL} \sim -8{,}700$ km/s (Figure 3e), suggesting a tail-side crossing of the X-line. B_M at the neutral line indicates a guide field B_g of 0.49 nT (horizontal line in Figure 3b), and the negative to positive sign change of B_M relative to B_g is consistent with the Hall magnetic field pattern on the tailward side of an X-line (Eastwood et al., 2013). Figure 4 shows the sketch of reconnection, and MMS are situated near the X-line (the red satellite-like symbol in Figure 4).

Figures 3f–3h present the three components of the measured electric field $\boldsymbol{E}$ and electron convection electric field $-\boldsymbol{V}_e \times \boldsymbol{B}$. Here, the measured electric fields are down sampled to 30-ms resolution. On the northern side of the current sheet, $\boldsymbol{E}$ and $-\boldsymbol{V}_e \times \boldsymbol{B}$ basically coincide with each other except for some fluctuation of $-\boldsymbol{V}_e \times \boldsymbol{B}$ probably due to low count-rate noise. From the high-speed electron flow interval at the southern side, the three

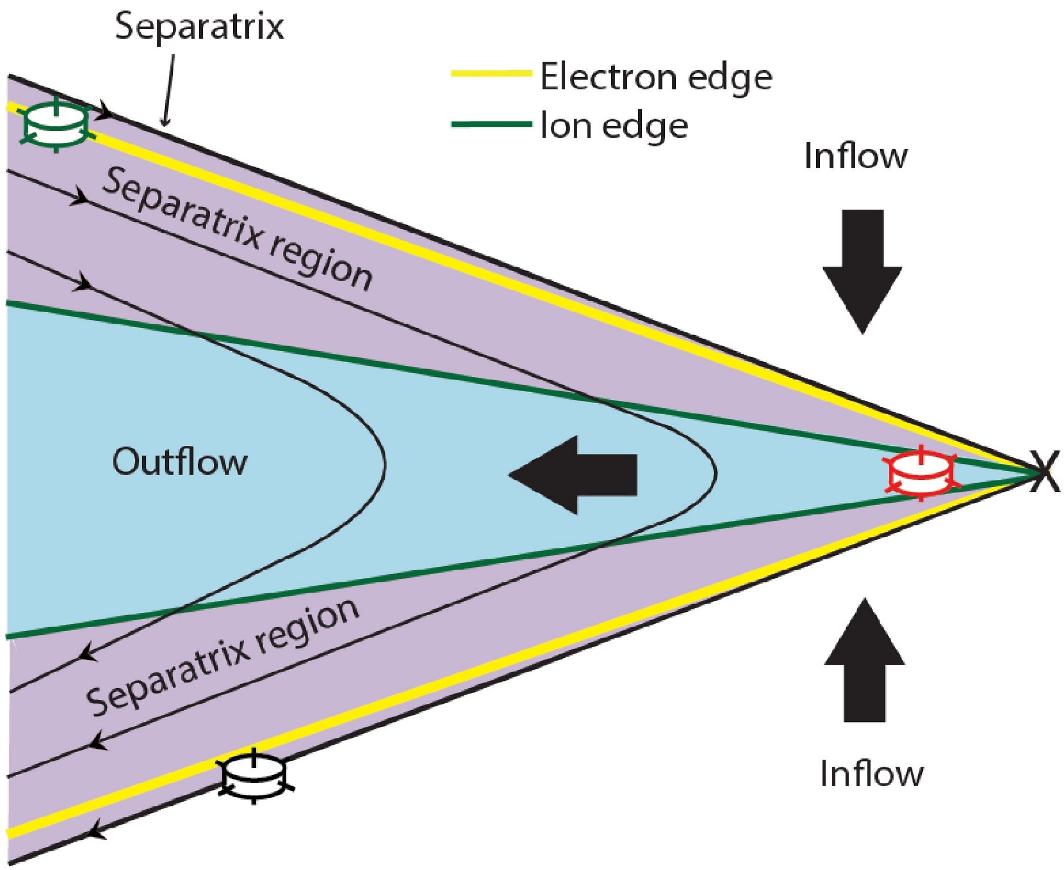

Figure 4. Sketch of reconnection in the magnetotail (modified from Lindstedt et al., 2009). The red, black, and green satellite-like symbols correspond to the locations of the satellites in the reconnection plane for the high-speed electron flow events shown in Figures 3, 5, and 6, respectively.

components of the two electric fields show large differences. As shown in Figure 3f, the measured E_L exhibits large-amplitude (~10 mV/m) quasi-electrostatic fluctuations, whereas $E_{\perp L}$ coincide with $-(\boldsymbol{V}_e \times \boldsymbol{B})_L$, indicating that the electrostatic fluctuations are predominantly contributed by the parallel component of $\boldsymbol{E}$. Taking the advantage of the fact that MMS1 and MMS2 are mainly separated along the **L** direction, we perform the timing analysis on the E_L component from those two spacecraft, revealing a fast (1,800 km/s) tailward propagation of those fluctuations, as illustrated by the magenta curve in Figure 3i. As B_M is ~0.49 nT and B_N is ~ -0.43 nT at the neutral line, those field-aligned propagating waves also exhibit large-amplitude perturbations in E_M (Figure 3g). On either side of the neutral line, $|-(V_e \times B)_N|$ is larger than the measured E_N, denoting overshoot motion of the electrons related with the magnetic field lines. The $(\boldsymbol{E} + \boldsymbol{V}_e \times \boldsymbol{B})_N$ is likely balanced by the normal gradient of the electron pressure term P_{eNN}, as well analyzed in another EDR event (Egedal et al., 2019).

On both sides of the current sheet, MMS observe large electron temperature anisotropy with $T_{e\|}/T_{e\perp}$ reaching ~2.8. Figures 3l and 3m present two examples of 2D reduced eVDFs in those regions, and their bi-directional features along the local magnetic fields demonstrate inflowing electrons of a magnetic reconnection site (L. J. Chen et al., 2008; Egedal et al., 2012, 2013). As MMS2 approaches the neutral line, the electron temperature anisotropy features gradually diminishes, and the eVDFs exhibit agyrotropy with respect to $\boldsymbol{E} \times \boldsymbol{B}$ drift (-1.5×10^4 km/s) (Figures 3j and 3k). Based on all those observations, we conclude that the high-speed electron flow in Figure 3 is associated with an EDR in the magnetotail, and the MMS crossing trajectories are illustrated in Figure 3i.

To estimate the current sheet thickness, we perform multi-spacecraft timing analysis of B_L, which yields a normal velocity $\boldsymbol{V}_N = 604 \times [0.26, 0.58, 0.77]$ km/s in GSE. This direction is well aligned (8.4°) with $\boldsymbol{N}$ from MVA-B. The normal spatial scale is estimated to be 199 km = 5.3 d_e for the time interval T_{HP}. Additionally, we employ a

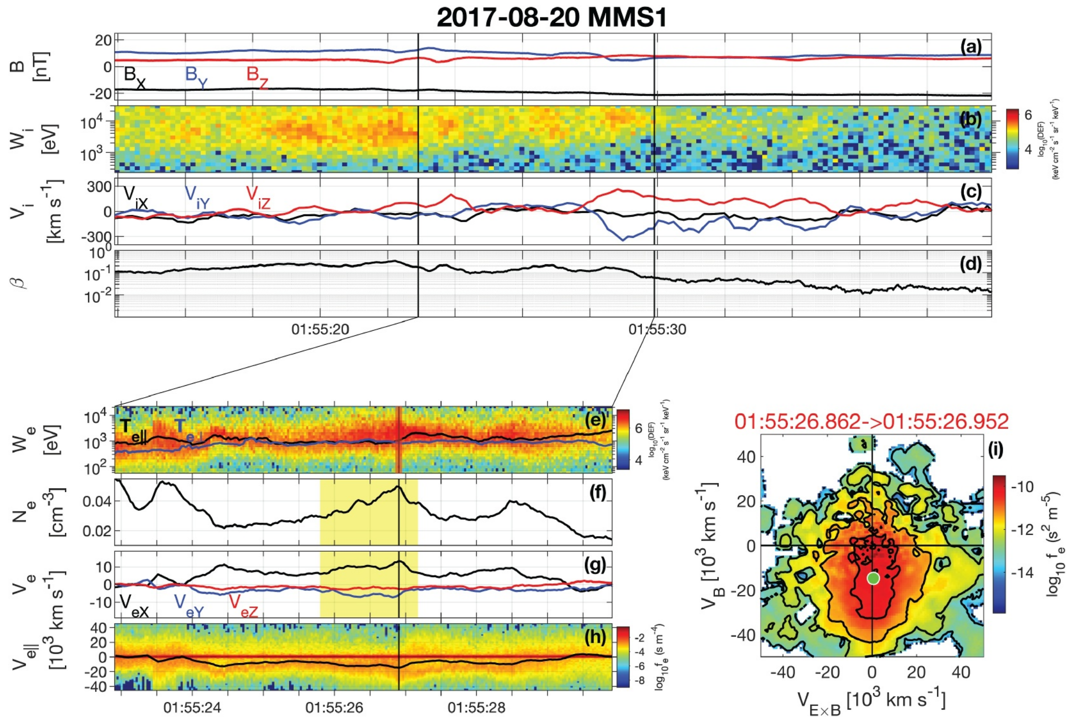

Figure 5. An HSEF example in plasma sheet boundary layer observed by MMS1 on 2017 August 20. (a) $\boldsymbol{B}$. (b) Ion energy flux. (c) $\boldsymbol{V}_i$. (d) Plasma beta β. Zoom-in plot: (e) Electron energy flux with $T_{e\parallel}$ (black), $T_{e\perp}$ (blue). (f) N_e. (g) $\boldsymbol{V}_e$. (h) Field-aligned eVDF after integral over the directions perpendicular to $\boldsymbol{B}$, with parallel electron bulk velocity $V_{e\parallel}$ (black curve). (i) 2D reduced eVDF in the $\boldsymbol{V}_{E\times B}$-$\boldsymbol{V}_B$ plane at the time of the HSEF speed peak, indicated by the red bar in panel (e). The green filled circle denotes the electron bulk velocity.

simple Harris current sheet fitting method (see W. Y. Li et al., 2021, for more details), which yields a full thickness of 5.8 d_e, consistent with the result above. In summary, MMS observe a high-speed electron flow at the electron-scale (5.5 d_e) current sheet of a magnetotail EDR.

3.2. Example 2: High-Speed Electron Flow in PSBL

The plasma sheet boundary layer is a temporally variable transition region located between the magnetotail lobe regions and central plasma sheet (Eastman et al., 1984). Commonly, PSBL comprises hot (~keV) plasma sheet ions, whose source is thought to be magnetic reconnection in the distant magnetotail, and cold (few eV) ions of ionospheric origin. Before the MMS era, the high-speed electron flows were inferred from the current density estimated by the magnetometer data (e.g., Ohtani et al., 1988). Those fast electrons carrying the currents were suggested to be responsible for various types of electrostatic fluctuations in the PSBL, for example, the electrostatic solitary waves (Matsumoto et al., 1994). With MMS, the three-dimensional eVDFs are fully resolved, and here we present an example of high-speed electron flows in the PSBL.

Figures 5a–5d illustrate a crossing of MMS1 from the PSBL to the lobe region on 2017 August 20. In the entire crossing, the magnetic field is dominated by negative B_X component, with the average $\boldsymbol{B}$ of [−19.9, 9.0, 5.5] nT, and a weak disturbance is observed from 01:55:21 UT to 01:55:30 UT. MMS1 continuously observes high-energy ions with energies exceeding 1 keV (Figure 5b) from 01:55:21 UT to 01:55:30 UT, accompanied by a plasma beta β of ~0.13 (Figure 5d). After 01:55:30 UT, the high-energy ions become less pronounced, and β gradually decreases to 0.03 (Figure 5d). All those observations indicate that MMS are initially located in the southern PSBL and subsequently enter the lobe region. During the transition, the spacecraft encounter several enhanced ion flows, for example, 430 km/s at 01:55:29 UT.

Within the interval marked by the two vertical black lines in Figures 5a–5d, MMS detect a high-speed electron flow, and the detailed observations are presented in Figures 5e–5h. Its peak speed (1.5×10^4 km/s) is captured by MMS1, with a duration of $T_{HP} = 1.38$ s, a number density of 0.05 cm^{-3}, and an electron temperature of 920 eV.

The high-speed electron flow predominantly moves along the $+\boldsymbol{X}$ direction (Figure 5g) and carries an intense parallel current, with a current density peak of 117 nA/m^2. This is consistent with the B_Y enhancement on the plasma sheet side and the B_Y decrease on the lobe side. Figure 5h shows the field-aligned eVDF after integrating over the perpendicular directions. One can see that large electron bulk speeds originate from the motion of the entire electron distribution functions rather than from a sole extremely fast electron beam. Figure 5i displays the 2D eVDF at the velocity peak, showing an entire anti-parallel drifting motion along the local magnetic field. Around the current event, MMS cross the separatrix back and forth and observe thermalized electrons (not shown). The eVDF shown in Figure 5i is consistent with the inflow electrons accelerated by the electrostatic potential in the inflow side of the separatrix (Egedal et al., 2015; Norgren et al., 2020). For the observations in Figure 5e, electrons exhibit some temperature anisotropies, with $T_{e\parallel} > T_{e\perp}$, while no significant plasma waves are observed here. To sum up, MMS capture a high-speed electron flow moving antiparallel to the ambient magnetic field at the separatrix (the black satellite-like symbol in Figure 4), which is corresponding to the inflow electron and carries a substantial field-aligned current.

3.3. Example 3: High-Speed Electron Flow in Lobe Region

In the magnetotail, the lobe region is located between the plasma sheet boundary layer and the magnetopause. The lobe magnetic field is anchored in the polar cap ionosphere and is open to the interplanetary space (Chappell et al., 1987, 2000; Shi et al., 2013). Any energetic particles can quickly either penetrate into the ionosphere or escape into the interplanetary space, leaving nearly stagnant cold plasmas of ionospheric origin in the open magnetic field lines. The magnetic field amplitude is typically tens of nT and varies under different interplanetary magnetic fields, solar wind dynamics, radial distances, and geomagnetic activity (Nakai et al., 1991; Shukhtina et al., 2004; Tsyganenko, 2000). The lobe plasma number density is on the order of 0.01 cm^{-3} (Gosling et al., 1985; Haaland et al., 2008, 2017). Limited by the electron instrument capability before MMS, the electron dynamics in the lobe region lacks detailed analysis.

Figure 6 presents an example of the high-speed electron flows in the northern lobe observed by MMS3 on 2017 June 11. As shown in Figure 6a, the quiet magnetic field is approximately along $+\boldsymbol{X}$ direction, with an average $\boldsymbol{B}$ of [33.8, 1.1, 1.2] nT in GSE. MMS observe cold ions of ionospheric origin and negligible high-energy (several to tens of keV) ions (Figures 6b and 6c). The average number density is 0.02 cm^{-3} (Figure 6d) and the cold-ion motion is slow (Figure 6e). All those space features demonstrate that MMS are in the northern lobe region. In addition, MMS observe a tailward ion jet ($V_{iX} \sim -380$ km/s, not shown) around the current event.

Figures 6f and 6h present zoom-in plot of the electron observations in the time interval denoted by the two vertical black lines in Figures 6a–6e. Figure 6f shows that cold electrons are observed from 17:25:15.2 UT to 17:25:15.9 UT, consistent with the electron features in the lobe region. Then, electron energy and temperature increase in the yellow-shaded region, and MMS observe a HSEF with peak speed (7,600 km/s) captured by MMS3 at 17:25:16.2 UT (vertical black line). The large bulk speed comes from the motion of entire eVDF, accompanied with an unambiguous temperature anisotropy, as shown in Figures 6h and 6m. This HSEF is predominately earthward and along the ambient magnetic field lines, consistent with the cold inflow electrons of reconnection. From the V_{eX} reversal, in addition to the cold parallel electron beams, MMS observe hot anti-parallel electrons (Figures 6h and 6n), which are consistent with the reconnection outflow electrons. At 17:25:16.60 UT, MMS3 observes fast tailward electron flow with a peak speed reaching 4,100 km/s (vertical green line in Figures 6f–6h), meaning that the hot electrons (as shown in Figure 6o) are dominant population there. After the tailward flows, MMS enter a region with stagnant hot electrons (Figures 6f, 6h, 6p). Based on all those observations, MMS3 captures a HSEF in the transition layer with the lobe parameters, and this layer is probably associated with the electron edge of the reconnection separatrix layer (the green satellite-like symbol in Figure 4).

Meanwhile, intense electric field fluctuations are observed with amplitudes reaching 100 mV/m around the V_{eX} reversal, and Figures 6i–6l show details of the wave properties. The frequencies of those broadband quasi-electrostatic fluctuations are between the ion plasma $\left(f_{pi}\right)$ and electron cyclotron $\left(f_{ce}\right)$ frequencies. Those fluctuations have both parallel and perpendicular components, while $E_\parallel$ exhibits bipolar feature and $E_\perp$ does not show unambiguous organized patterns. Similar $\boldsymbol{E}$ fluctuations are observed by the other three spacecraft as well. MMS1 and MMS2 are separated mostly along the $\boldsymbol{X}$ direction or local magnetic field direction and observe nearly identical $\boldsymbol{E}$ fluctuations. Thus, we use a timing analysis between MMS1 and MMS2 to estimate the phase speed, which is approximately 2.2×10^4 km/s parallel to $\boldsymbol{B}$. The estimated phase speed is close to the parallel beam

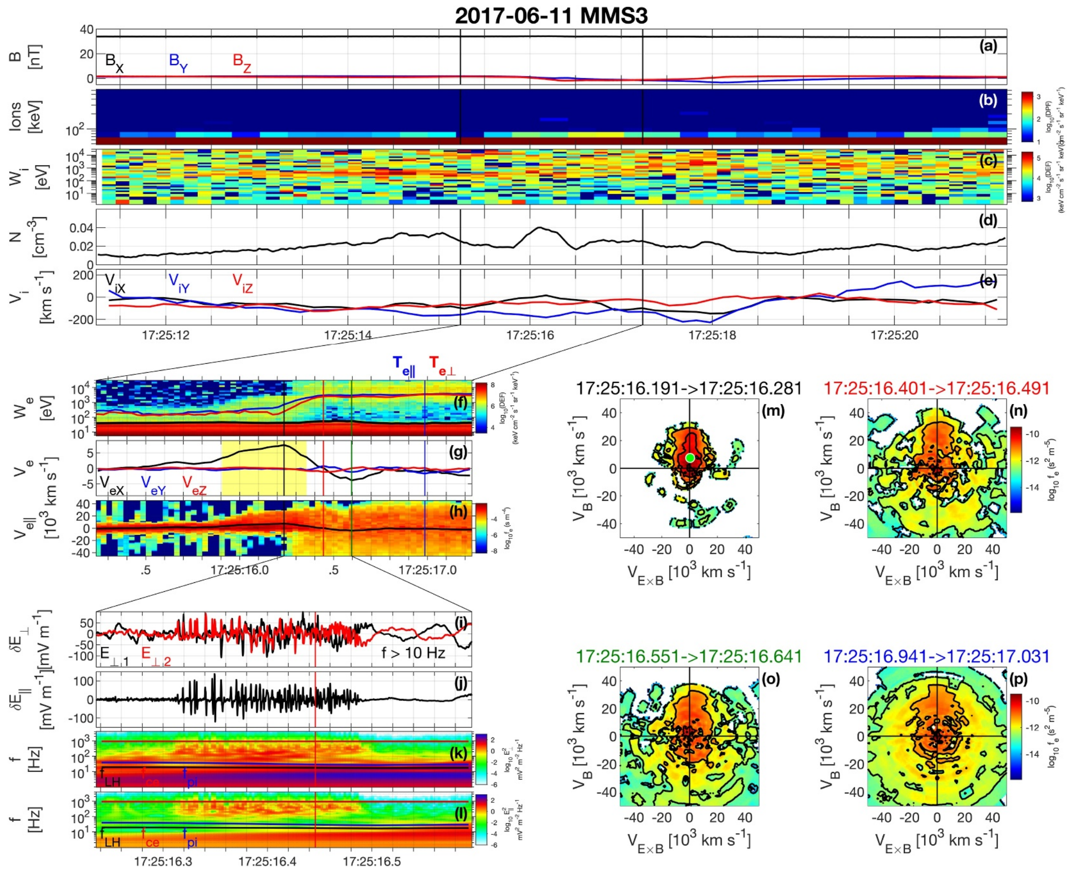

Figure 6. An HSEF example in the lobe region observed by MMS3 on 2017 June 11. (a) $\boldsymbol{B}$. (b) Energetic ions by FEEPS. (c) Ion energy flux by FPI. (d) N_e. (e) $\boldsymbol{V}_i$. Zoom-in plot from 17:25:15.2 UT to 17:25:17.2 UT: (f) Electron energy flux with $T_{e\parallel}$ (blue), $T_{e\perp}$ (red) and spacecraft potential (black). (g) $\boldsymbol{V}_e$. (h) Field-aligned eVDF, with electron parallel velocity $V_{e\parallel}$. (i) Perpendicular and (j) parallel electric field waveforms in magnetic field-aligned coordinates after being high-pass filtered (f>10 Hz). Power spectra of the (k) perpendicular and (l) parallel electric fields. The black, red, and blue curves represent the low-hybrid (f_{LH}), electron cyclotron (f_{ce}), and ion plasma (f_{pi}) frequencies. The vectors in panels (a), (e) and (g) are presented in GSE. The red vertical line in panels (f)–(l) corresponds to the electron flow reversal. (m)–(p) 2D reduced eVDFs in the $\boldsymbol{V}_{E\times B}$-$\boldsymbol{V}_B$ planes at the times of the HSEF speed peak, reversal, reversed peak, and the hot electrons.

speed in Figure 6o, suggesting that those large-amplitude quasi-electrostatic fluctuations are likely driven by the cold inflow electrons with strong interaction with the hot outflow electrons. The wave-beam interaction may thermalize those fast cold beams (see Figure 6p as an example). More detailed analysis will be performed in the future with multiple case comparison. In summary, we present an example of field-aligned high-speed electron flows in the northern lobe region. Those electron flows are associated with the reconnection electron edge where the interaction of the inflow and outflow electrons generate large-amplitude quasi-electrostatic waves.

4. Statistics Results

In this section, we investigate the statistical results of the high-speed electron flows, and we will refer to it as HSEF in short. In Section 4.1, we present the properties of basic plasma parameters, including time-scale, number density, and electron bulk velocity. In Section 4.2, we investigate the spatial distributions in the Earth's magnetotail. In Section 4.3, we distinguish the PS, PSBL and lobe under different plasma and magnetic field environments, and the characteristics of electron flow motions and their relation with reconnection are analyzed in Section 4.4.

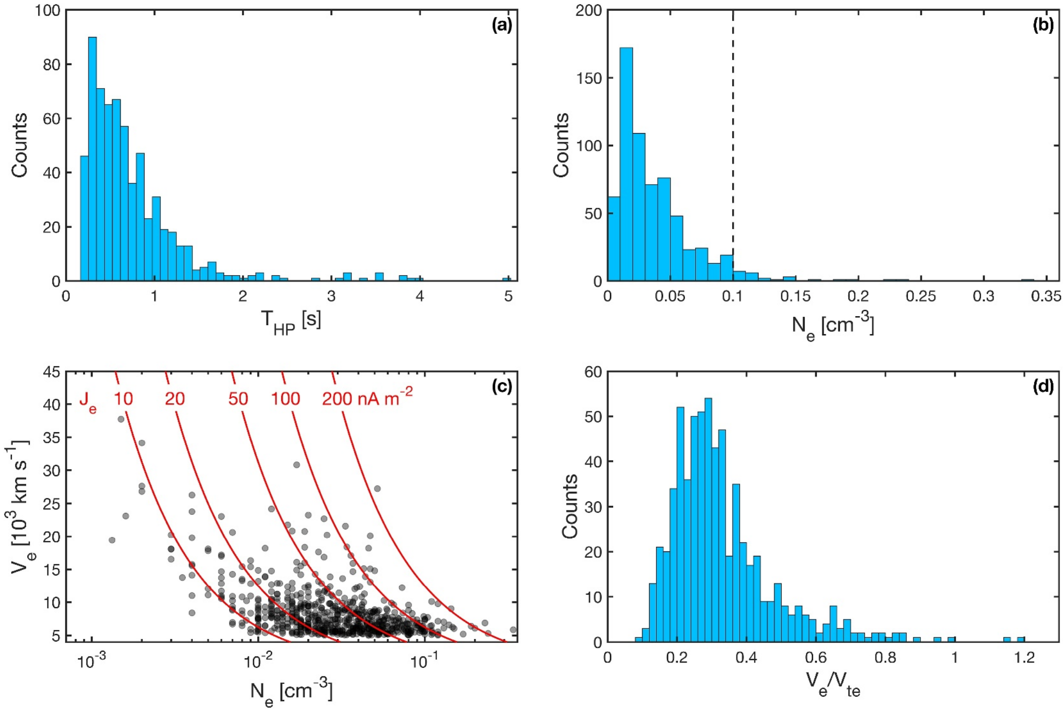

Figure 7. HSEF basic plasma parameters. Histograms of panel (a) T_{HP}, (b) N_e. (c) Scatter plot of N_e and V_e. The five red curves represent the contours of the electron current density $(J_e = -q_e N_e V_e)$ at values of 10, 20, 50, 100, and 200 nA/m^2, respectively. (d) Histograms of V_e/V_{te}, where V_{te} represents the electron thermal speed.

4.1. Basic Plasma Parameters

Figure 7 displays the statistical results of three basic plasma parameters of HSEFs. As shown in Figure 7a, the event counts basically decrease with the duration of the HSEFs, and the average T_{HP} is 0.74 s. The shortest duration is 0.18 s, corresponding to 6 data points by FPI. 93% of the events have duration shorter than 1.5 s, which is shorter than the typical time scale (2.8 s) of the electron jets reported by S. Y. Huang et al. (2020). This difference is mainly from different event selection criteria, where S. Y. Huang et al. (2020) focused on the electron jet events with speeds in the range of 500–2,000 km/s. In our event list, there are 23 events with T_{HP} larger than 2 s, and the largest one is 4.95 s. All those long-duration events are observed in the plasma sheet and lobe regions. Figure 7b shows the histogram of the electron number densities at the speed peaks. The whole distribution exhibits a declining trend toward large N_e. The lowest N_e is 0.0013 cm^{-3}, and the highest one is 0.34 cm^{-3}. The average N_e is 0.038 cm^{-3}, and 95% of those events have N_e lower than 0.1 cm^{-3} (black dashed line in Figure 7b). The previous statistical study by S. Y. Huang et al. (2020) focused on events with densities larger than 0.1 cm^{-3}, while several reported EDR and separatrix events have HSEFs with number densities around 0.05 cm^{-3} (W. Y. Li et al., 2021; Norgren et al., 2020; Torbert et al., 2018), indicating the importance of low-density HSEFs. Our survey here gives a nearly complete event list of HSEFs with speeds over 5,000 km/s in the Earth magnetotail by MMS. Further studies will be performed to examine events below 5,000 km/s.

Figure 7c displays the scatter plot between V_e and N_e. The average speed of all events is 8,721 km/s, and 78% of the selected events have speeds between 5,000 km/s and 1×10^4 km/s. There are four high-speed electron flow events with speeds exceeding 3×10^4 km/s (0.1 times of the speed of light). Two of them are associated with EDR, and the other two are located in the lobe regions. Figure 7c shows a trend that higher speed events have lower number densities, which is similar with the trend of BBFs (Grigorenko et al., 2012; Y. D. Ma et al., 2009). The five red curves in this panel represent the contours of the current density contributed by electrons (J_e) at values of 10, 20, 50, 100, and 200 nA/m^2. In the Earth magnetotail, the densities of cross-tail current are 5–10 nA/m^2 (Rong et al., 2011). Here, 71% of the events carry J_e exceeding 20 nA/m^2, and 6.4% have Je over 100 nA/m^2. Those intense current densities may relate with extremely strong electron-scale processes in the magnetotail, including the reconnection EDRs. Figure 7d shows the histogram of normalized electron speed V_e/V_{te} (V_{te} is the

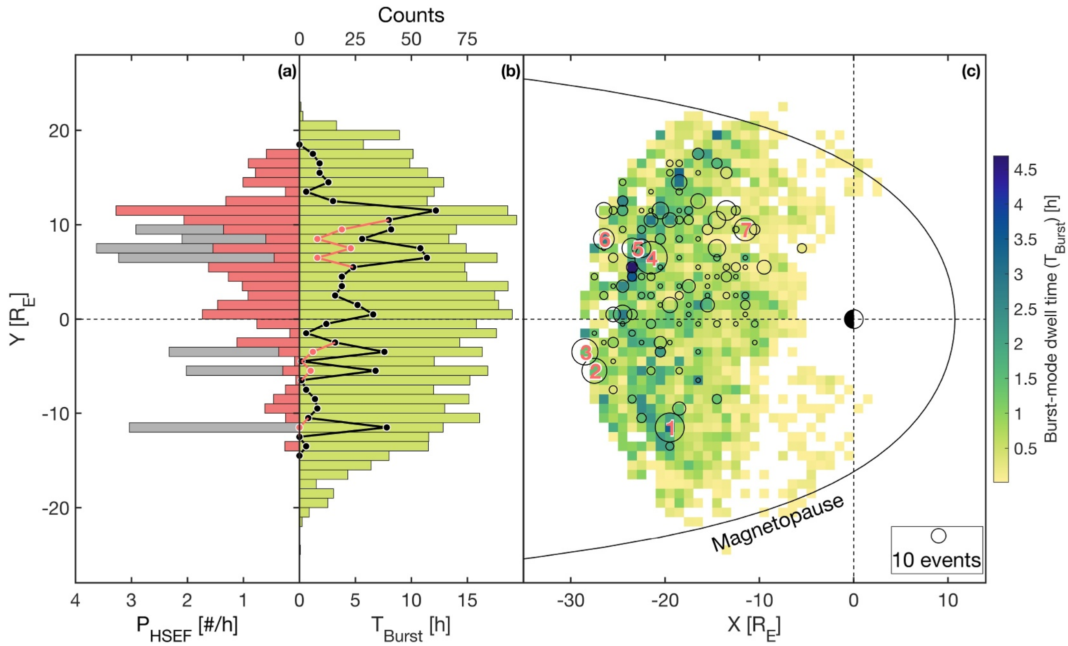

Figure 8. HSEF dawn-dusk asymmetry. (a) Histogram of the HSEF observation probability P_{HSEF} during burst-mode operation along GSE-Y. (b) HSEF event counts and histogram of MMS burst-mode dwell time T_{Burst}. (c) HSEF event counts and 2D histogram of T_{Burst} in the X-Y plane. The black curve shows the nominal magnetopause location by Shue et al. (1998) and the circles represent event counts, normalized by their area. The numbers (1–7) highlight continuous events (>20) within one-orbit observations. The gray histogram in panel (a) and the black line in panel (b) represent the total observation probabilities and the total event counts, respectively. The red histogram in panel (a) and red line in (b) show the results without those continuous events. The bin size in panels (a)–(c) is 1 R_E.

electron thermal speed), and the minimum V_e/V_{te} is 0.1. 63.7% of the events have speeds between 0.2 V_{te} and 0.4 V_{te}, and the V_e/V_{te} have the highest count at 0.26. Notably, there are two HSEF events with $V_e > V_{te}$ and both of them are associated with EDRs (Qi et al., 2024; Torbert et al., 2018).

4.2. Spatial Distribution

The spatial distribution and observation probability (P_{HSEF}) of the HSEF events are presented in Figures 8 and 9. Firstly, in the X-Y plane, the event counts are illustrated by the circles in Figure 8c, with 2D histogram as a background showing the MMS burst-mode dwell time (T_{Burst}) in the magnetotail. MMS employ automated burst-mode triggers onboard the spacecraft and a Scientist-In-The-Loop (SITL) system on the ground to select intervals for which burst mode data is down-linked, including magnetic reconnection, turbulence, and plasma waves (Argall et al., 2020). As shown in Figure 8c, MMS collect burst-mode data when the spacecraft are roughly 10 R_E away from the Earth center and have nearly full coverage of the middle magnetotail within the investigated five years. Note that MMS increased its apogee from 25 R_E to 28 R_E in 2019, which produces the large T_{Burst} stripe around 25 R_E in Figure 8c. In addition, the magnetosheath and the solar wind intervals in the analyzed months are removed manually based on the plasma and magnetic field parameters. The total T_{Burst} of the 5 years in the magnetotail is 515 hr. As shown by the histograms in Figures 8b and 8c, MMS have the burst-mode selection mostly in the central magnetotail and less selection toward the magnetopause boundary. As shown by the green histogram in Figure 8b, the burst-mode selection is nearly symmetric between the dawn (226.1 hr, 44.2%) and dusk (288.6 hr, 55.8%) sides, while the HSEF events exhibit a strong dawn-dusk (26.3%–73.7%) asymmetry. We have also analyzed the spatial distribution of the HSEFs in different coordinate systems (not shown), including aberrated (Nagai et al., 1998) GSE, Geocentric Solar Magnetospheric (GSM), and aberrated GSM coordinate systems. The burst-mode dwell time remains roughly dawn-dusk symmetric, with a clear dawn-dusk asymmetry of the HSEFs persisting, where the dusk-side event proportion stays around 70%. Additionally, by varying the CC constraints, we find that both the HSEF event counts and the dawn-dusk proportion remain approximately constant (not shown), indicating that the HSEF dawn-dusk asymmetry (30%–70%) is robust. The black line in

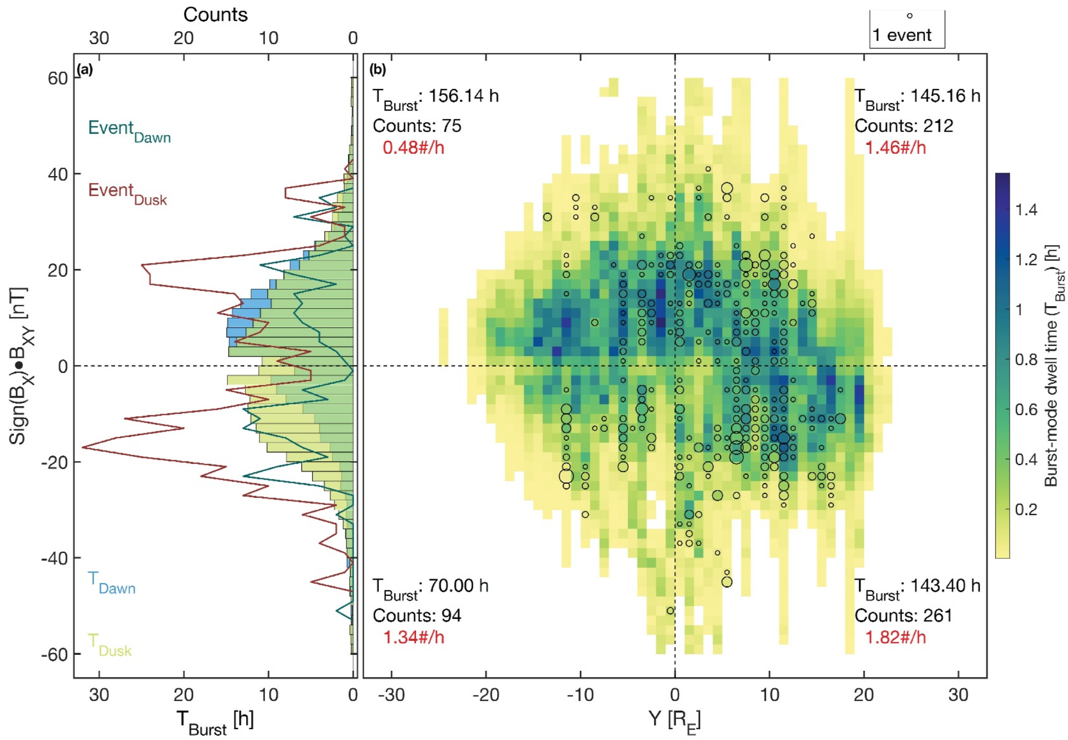

Figure 9. HSEF space distribution in Y-$Sign(B_X)\,B_{XY}$ plane. (a) Histogram of T_{Burst} on dawn (blue) and dusk (yellow) sides and event counts on the dawn (green curve) and dusk (red curve). Note the overlap of the blue and yellow histograms is in green color. (b) HSEF event counts and T_{Burst} in the Y-$Sign(B_X)\,B_{XY}$ plane. Here, $B_{XY} = \sqrt{{B_X}^2 + {B_Y}^2}$, and the bin size is 1 $R_E \times 2$ nT. T_{Burst}, event counts, and observation probabilities of the four quadrants are labeled in the corners.

Figure 8b displays the event counts along Y, and the corresponding observation probabilities are presented by the gray bars in Figure 8a. The dusk side (1.65 #/h) has a much larger observation probability than the dawn side (0.74 #/h).

One may note several peaks in the counts and observation probability in Figure 8. These are contributed by several clustered events, and the magenta numbers (1–7) in Figure 8c label those cases with more than 20 HSEF events for a continuous burst-mode collection. The detailed information of those seven cases are listed in Table 1, and three of them are located in the dawn-side magnetotail. Basically, those cases are encountered when the geomagnetic activity level is high, and are all locally associated with turbulent magnetotail and reconnection. For example, the 2017 July 26 case was carefully analyzed by Ergun et al. (2020a, 2020b), showing tens of intense current sheet crossings in the reconnection-driven turbulence and unambiguous features of local particle acceleration. The total T_{Burst} of the seven cases is 3.57 hr (0.7% of all T_{Burst}), while the HSEFs from those seven intervals contribution 34.5% of all event counts. Whether MMS can capture this type of active events is random.

Table 1
List of 7 Intervals With Continuous HSEF Events With ≥20 Cases

Case	Date	Time interval	X_{GSE} (R_E)	Y_{GSE} (R_E)	Z_{GSE} (R_E)	SME (nT)	Counts
1	2017-05-28	03:55–04:06	−19.3	−11.4	3.2	2,037	39
2	2020-08-03	01:04–01:28	−27.5	−5.1	−0.8	1,048	29
3	2020-08-02	16:46–17:13	−28.1	−3.6	2.6	591	32
4	2019-09-06	04:34–05:12	−21.8	6.3	1.6	934	49
5	2017-07-26	07:24–07:36	−23.0	7.7	5.0	1,359	31
6	2020-08-26	21:49–23:59	−26.3	8.5	3.4	392	20
7	2020-08-29	09:54–10:28	−11.8	9.2	6.6	747	22

To exclude the bias of event encountering and selection, we show the event counts (red line in Figure 8b) and observation probability (red bar in Figure 8a) without those clustered cases. The dawn-dusk asymmetries of the HSEF events (16%–84%) and the observation probability (0.3 #/h-1.2 #/h) become more distinct after removing the clustered cases. This asymmetry and the peak observation probability around Y ~ 10 R_E are similar with the spatial properties of BBFs (Lotko et al., 2014; Nagai et al., 2013), IDRs (Lu et al., 2018; Rogers et al., 2023), flux ropes (Imber et al., 2011), and DFs (Liu et al., 2013; Xiao et al., 2017), suggesting that the HSEF analyzed in this study may be closely associated with magnetotail reconnection. Nagai et al. (2023) found that the magnetic reconnection also exhibits dusk-side preference, and its spatial distribution closely matches that of the HSEFs, further strengthening the relation between the HSEFs and magnetic reconnection.

The plasma parameters and magnetic field topology exhibit large differences along the normal direction of the magnetotail neutral sheet. To investigate the HSEF distribution along the normal direction, we adopt $Sign(B_X)\,B_{XY}$ as an indicator of the normal distance to the neutral sheet, where B_{XY} is $\sqrt{B_X{}^2 + B_Y{}^2}$, and the positive and negative signs of B_X denote the northern and southern sides of the neutral sheet, respectively. The histogram in Figure 9 presents the MMS T_{Burst} in the Y-$Sign(B_X)\,B_{XY}$ plane, which has a large $Sign(B_X)\,B_{XY}$ coverage from −60 to 60 nT. In Figure 9b, the distribution of high T_{Burst} regions (bluish bins) is accompanied with the drifting spacecraft apogees. The burst-mode dwell time, the event counts, and the observation probabilities of the four quadrants are labeled in the corners. Due to the MMS apogee drift, the dwell time in the southern-dawn magnetotail is nearly half of those in the other three quadrants. The HSEF events are mostly observed on the dusk quadrants, and the southern-dusk one has the largest observation probability, which is caused by a combination of the dawn-dusk asymmetry and the continuous cases 4–7. Figure 9a shows the 1D histogram of T_{Burst} and the HSEF events in the dawn and dusk magnetotail. We find that 15 events are observed within ± 2 nT, which are directly related with the electron-scale current sheet. One can find observation probability peaks at −17 nT in the southern side and 21 nT in the northern side, indicating that the HSEFs are most frequently observed in the PSBL and/or lobe region. Raj et al. (2002) found that the field-aligned beams in the PSBL are also concentrated near ±20 nT, which is consistent with our statistical results. Next, we will analyze the properties of HSEFs in different magnetic filed and plasma environments.

4.3. Flow Characteristics in Different Regions

In the Earth's magnetotail, the magnetic field magnitude (e.g., B_{XY}) is not sufficient to distinguish the plasma sheet, PSBL, and lobe regions (Boakes et al., 2014; Grigorenko et al., 2012). Vo et al. (2023) conducted a statistical study of the plasma and magnetic field parameters of the magnetotail using the MMS observations from 2017 to 2020. They combined the ion data from FPI (~10 eV–30 keV, Pollock et al., 2016) and FEEPS (60–500 keV, Blake et al., 2016; Mauk et al., 2016) to estimate the ion number density and thermal pressure. They characterized that the three different regions as follows: plasma sheet, $\beta_i \geq 0.2$ and $B_{XY} \leq 14$ nT; PSBL, $\beta_i \geq 0.2$ and $B_{XY} > 14$ nT; lobe, $\beta_i < 0.2$. In our study, we only use the FPI plasma moment data, which give smaller ion beta (usually by a factor of 2, Vo et al., 2023). Thus, we adopt the threshold conditions of $\beta_i = 0.1$ and $B_{XY} = 14$ nT. Figure 10 presents the distribution of the HSEF events in the β_i-$Sign(B_X)\,B_{XY}$ domain, and 254, 186, and 202 events are observed in the PS, PSBL, and lobe region, respectively. The color of each filled-circle in Figure 10 represents the peak electron bulk speed, revealing a widespread distribution of HSEF speeds across various regions in the magnetotail. For all those cases, β_i ranges from 0.003 to 133.3. In the lobe region, 13 cases have $\beta_i <$ 0.01, all with number densities lower than 0.02 cm^{-3}. In the plasma sheet, we find 26 events with $\beta_i > 10$, indicating encounters of intense electron-scale current sheets or diffusion regions.

Figure 11 presents the HSEF distribution in terms of θ and $Sign(B_X)\,B_{XY}$. Here, the horizontal axis θ represents the angle between the electron bulk velocity and $\boldsymbol{B}$, and the results in PS, PSBL, and lobe are denoted with the purple, blue, and orange filled circles, respectively. The HSEF events are quasi-symmetrically distributed on the northern and southern sides of the neutral sheet in the PS (44%–56%), PSBL (41%–59%), and lobe regions (51%–49%), respectively. In the PS, the HSEF directions distribute arbitrarily with the ambient magnetic field. Those high-speed electron flows could be generated by reconnection and be located in different regions, including reconnecting current sheet (W. Y. Li et al., 2021; Torbert et al., 2018; Zhou et al., 2019), separatrices (Norgren et al., 2020), flux ropes (X. Li et al., 2023; Wang et al., 2023), and DFs (Marshall et al., 2020). The 10 bigger filled circles in Figure 11 represent the events associated with the reported EDRs, and the HSEFs in those events mainly move quasi-perpendicular to the local magnetic field, with 9 events having $\theta \in [45°, 135°]$. Additionally, We

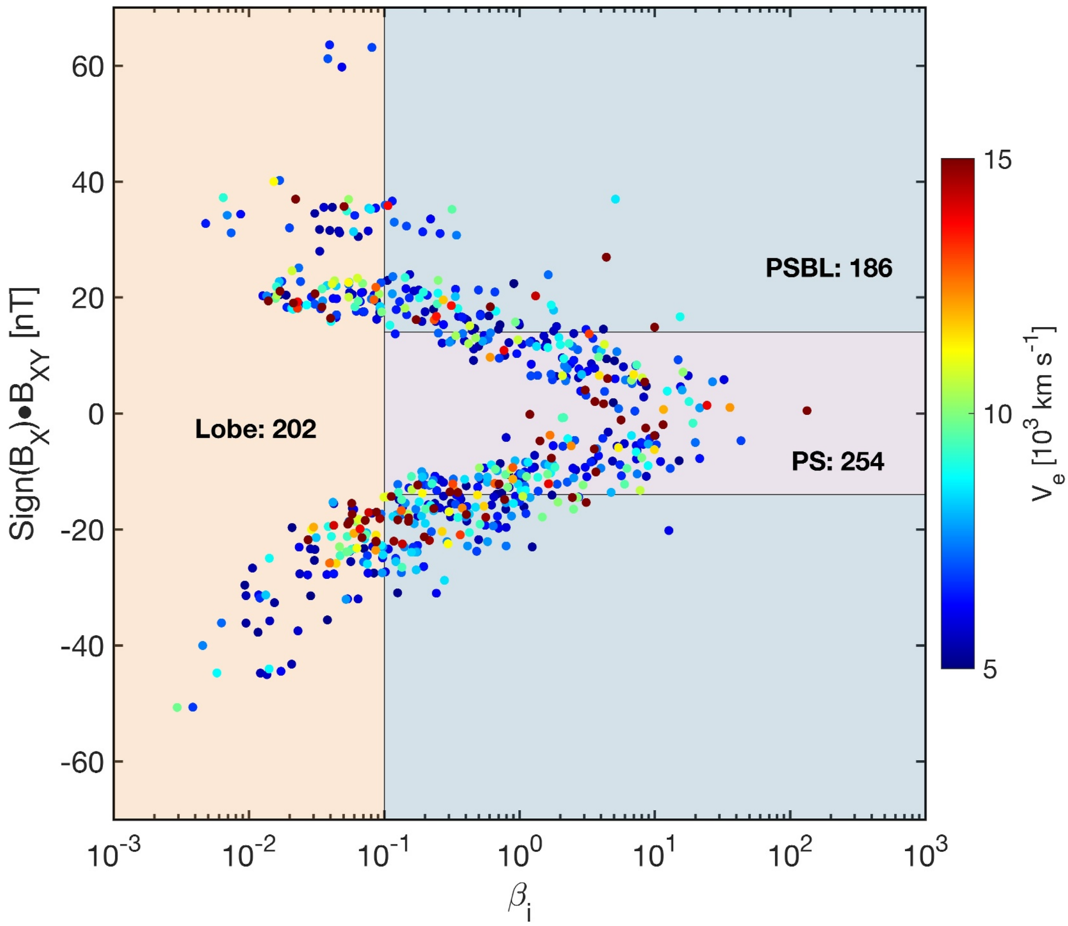

Figure 10. HSEF distribution in the PS, PSBL, and lobe region. PS is characterized by $\beta_i \geq 0.1$ and $B_{XY} \leq 14$ nT, and PSBL is characterized by $\beta_i \geq 0.1$ and $B_{XY} > 14$ nT. The lobe region is characterized by $\beta_i < 0.1$. 254, 186, and 202 events are observed in the PS, PSBL, and lobe regions, respectively, and the events are colored by V_e. Here, the β_i is 5-s average around the HSEF speed peak.

find more than 20 new EDR candidates from the PS HSEFs, including the one presented in Figure 3. All those EDR events give us an opportunity to investigate the statistical properties of EDRs under variations plasma and magnetic field inflow conditions. In the PSBL and lobe region, the HSEF events are predominately field-aligned with the local magnetic field, where 94% of the events are confined within 30° to the field-aligned directions. The larger bulk speeds of those events are associated with the motion of the entire eVDFs along the magnetic field or extremely fast electron beams.

4.4. Relation With Magnetic Reconnection

In order to investigate the relation between the HSEFs and magnetic reconnection, we present the HSEF directions in V_{iX}-$Sign(V_{eX})\,B_{XY}$ plane for the PS, PSBL, and lobe events, respectively, as shown by the three rows in Figure 12. We divide the HSEF events into four quadrants based on their X components of the ion and electron bulk velocities: in quadrant 1, we define $V_{eX} > 0$ and $V_{iX} > 200$ km/s as Regime EE; in quadrant 2, we define $V_{eX} > 0$ and $V_{iX} < -200$ km/s as Regime TE; in quadrant 3, we define $V_{eX} < 0$ and $V_{iX} < -200$ km/s as Regime TT; in quadrant 4, we define $V_{eX} < 0$ and $V_{iX} > 200$ km/s as Regime ET. Here, to eliminate the effect of the B_Y component near the dawn and dusk flank region, we only consider the HSEF events in the local time from 21 to 03 hr in Figure 12. Figure 12a displays the distribution of high-speed electron flows in the plasma sheet, while Figure 12b shows their electron temperature anisotropy ($T_{e\parallel}/T_{e\perp}$) along the normal direction of the neutral sheet, as indicated by $Sign(V_{eX})\,B_{XY}$. For the events in PS, 46% of them have tailward moving component, while the rest (54%) have earthward component (Figure 12a). The magnitudes of V_{iX} range from 0 to ~1,000 km/s, and 73% of

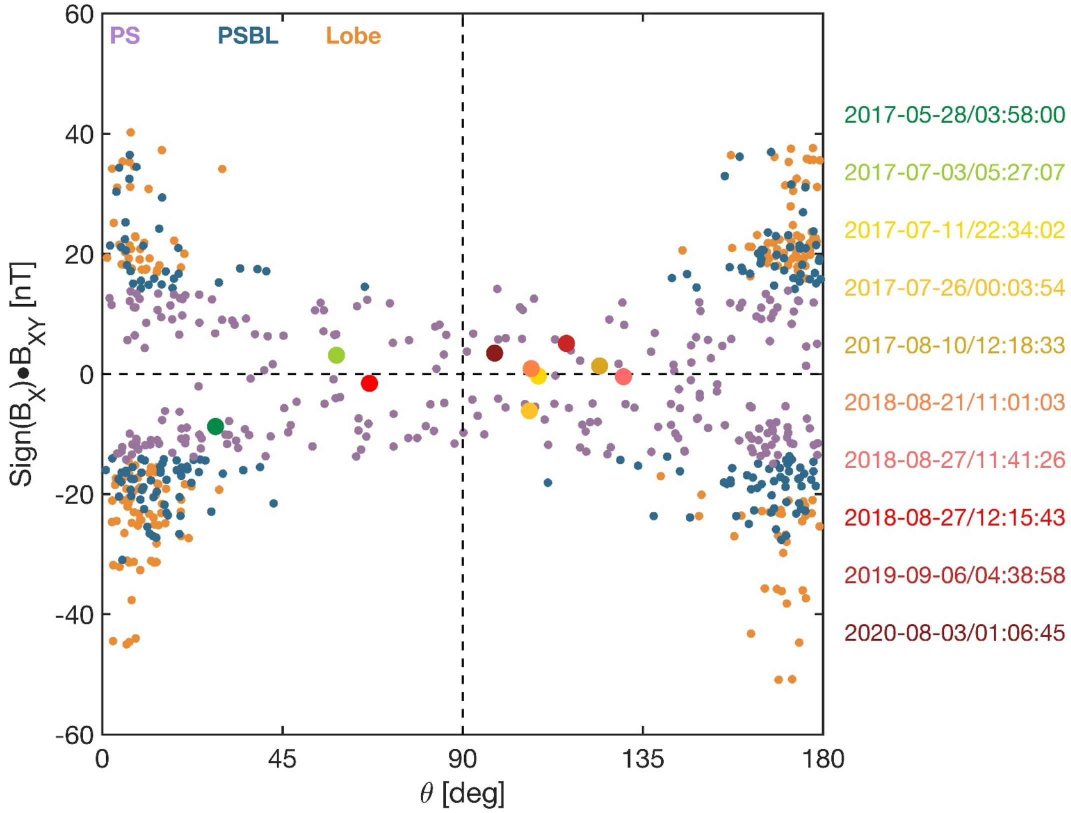

Figure 11. HSEF distribution in terms of θ and $Sign(B_X)\,B_{XY}$ in the PS (purple), PSBL (blue), and lobe region (orange), respectively. Here, the horizontal axis θ denotes the angle between the HSEF bulk velocity and **B**. The 10 bigger filled circles represent the events associated with the reported EDRs.

HSEF events are observed in unambiguous ion flows ($|V_{iX}| > 200$ km/s). 41 HSEFs are observed near the neutral sheet ($B_{XY} \leq 5$ nT) and exhibit arbitrary angles of motion with respect to the ambient magnetic field and nearly isotropic distribution functions ($T_{e\parallel}/T_{e\perp} \sim 1$). Notably, those events have large V_Y components (short lengths of the arrowed lines), contributing to the intense electron-scale current. Near the neutral sheet, 27 HSEFs are located in $|V_{iX}| > 200$ km/s, and 24 of them have the same earthward and tailward moving directions with ions, strongly implying that those events are super-Alfvénic electron outflow driven by reconnection. Away from the neutral sheet ($B_{XY} > 5$ nT), both tailward and earthward HSEF events are observed in the positive and negative ion flows. These events are predominately moving along the local magnetic field (blue and red circles in Figure 12a) and exhibit prominent electron temperature anisotropy ($T_{e\parallel} > T_{e\perp}$, with an average of 1.3). Additionally, several HSEFs move quasi-perpendicular to the local magnetic field (yellowish and light blue circles), and their perpendicular velocities are close to $\boldsymbol{E} \times \boldsymbol{B}$ drift velocities, indicating that those HSEFs are associated with reconnection separatrix layers.

The two panels in the second row of Figure 12 show the results in PSBL. Those HSEFs are mainly moving parallel or anti-parallel to the local magnetic field, and the large bulk speeds come from fast bulk motion of a single electron population (usually with bi-directional feature) or a combination of an extremely fast electron beam with a nearly stagnant background population, which exhibiting $T_{e\parallel}/T_{e\perp} > 1$ for most cases (Figure 12d). 70% of the PSBL-HSEF events are observed in Regimes TE and ET, and 30% of them are in Regimes TT and EE. Whether those events are corresponding to the reconnection inflow or outflow electrons needs future investigations. For the tailward HSEFs, only 4 events are located in Regime TT, which may be caused by the MMS apogee. The HSEF events in the tail side of an X-line is farther away from the Earth than in the Earth side, and tailward propagation high-speed electron flows will quickly leave away from the Earth. However, the apogee of MMS can only reach 28 R_E, causing the lack of the HSEF events in Regime TT.

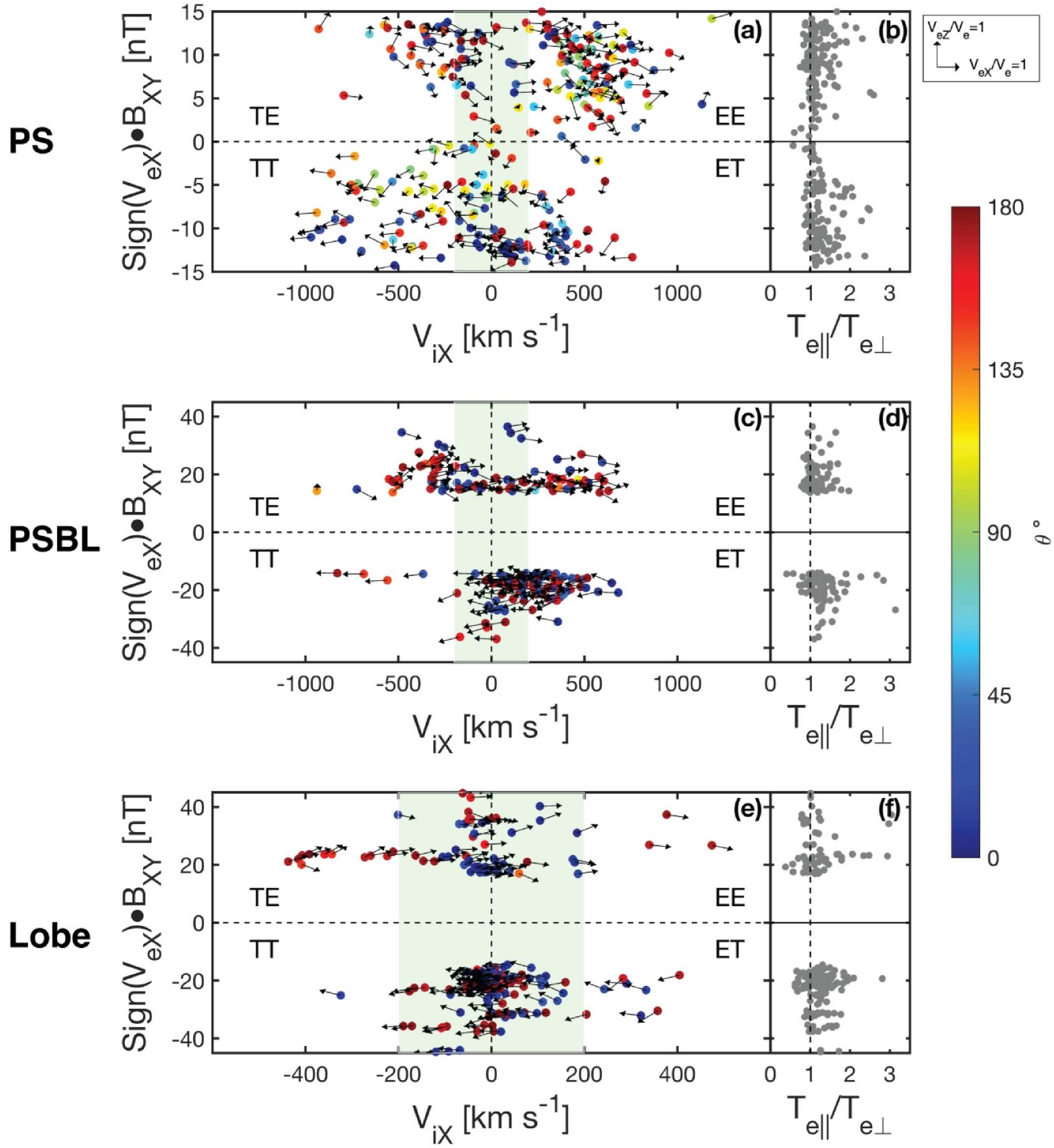

Figure 12. Relation between HSEF directions and ion flow directions. The three rows give the results of the HSEFs in PS, PSBL, and lobe, respectively. (a) Results of the HSEFs in the V_{iX}-$Sign(V_{eX})\,B_{XY}$ regime and (b) their $T_{e\|}/T_{e\perp}$. In V_{iX}-$Sign(V_{eX})\,B_{XY}$ panel, the arrowed lines represent the normalized V_{eX} and V_{eZ} by V_e, and each event is colored by θ. The green-shaded bars represent $|V_{iX}| \leq 200$ km/s. Here, the V_{iX} is 5-s average around the HSEF speed peak. In panel (b), the vertical dashed line represents $T_{e\|} = T_{e\perp}$. Panels (c) and (e) follow the same format as panel (a), and panels (d) and (f) follow same format as panel (b).

The bottom panels present the HSEF results in the lobes. Those events are symmetrically (51%–49%) distributed on both sides of the current sheet (not shown) and have similar motion features with the PSBL events. 87% of the HSEFs have $|V_{iX}| < 200$ km/s, consistent with the typical ion properties in the lobe region. As the example shown in Figure 6, those HSEFs observed in regions with lobe parameters may be correlated with the extended separatrix boundaries (outside of ion edges) of reconnection. The rest 24 HSEFs are observed in ion flows, and 20 of them are in Regime TE and Regime ET, indicating inflowing electron features. Figure 12f shows that 73% of the HSEFs have $T_{e\|} > T_{e\perp}$. For the remaining 27% events, tens of them have beam-like eVDFs, and those beams exhibit distinct $T_{e\|} < T_{e\perp}$. Graham et al. (2023) showed that this type eVDFs may be the source of upper hybrid waves (UHWs) in the magnetotail.

5. Conclusions

In this paper, we investigate high-speed electron flows in the magnetotail from 2017 to 2021. Utilizing FPI partial moments data, we establish stringent selection criteria and have identified 642 events. Those events exhibit a wide distribution across various regions, including EDR candidates, PS, PSBL, and lobe regions. We conduct a comprehensive statistical analysis of these high-speed electron flows, including the plasma parameters, spatial distribution, and flow direction characteristics in different regions. This study also analyses the relation between the HSEF events and magnetic reconnection.

The average time scale T_{HP} of HSEF events is 0.74 s, which is much shorter than the BBFs (10 minutes, Cao et al., 2006) in the Earth magnetotail, indicating the different dynamics between the high-speed electron flows and ion flows. Also, it is shorter than the duration of electron jets (2.89 s) observed by S. Y. Huang et al. (2020), because we focus on the electron flows with higher speed than them. 95% of events have N_e less than 0.1 cm^{-3}, and with the decrease of N_e, the electron speed shows a increasing trend, which is similar features with the ion flows in the magnetotail (Angelopoulos et al., 1992; Grigorenko et al., 2012; Kaufmann et al., 2005; Y. D. Ma et al., 2009). Y. D. Ma et al. (2009) found that the speed of earthward ion flow bursts was proportional to the Alfvén speed, and inversely proportional to the number density in naturally. Kim et al. (2010) found that the lower density flux tube will be affected by the stronger magnetic buoyancy force, then contribute a higher speed of the ion flow bursts. Electrons as the main carrier of current, high speed electron flows will spread out the electrons, thus resulting in a decreased density. The speed of HSEF events is concentrated between 0.2 V_{te} and 0.4 V_{te}, and the counts of HSEFs peak at 0.26 V_{te}.

The HSEF events exhibit strong dawn-dusk (30%–70%) asymmetry, and the observation probability on the dusk side (1.65 #/h) is about twice of that on the dawn side (0.74 #/h). The MMS burst-mode data are selected by the Scientist-in-the-Loop (SITL) on the ground, based on their understanding of important processes throughout Earth's magnetosphere (Argall et al., 2020). While the quasi-symmetric burst-mode dwell time ensures that the dawn-dusk asymmetry of the observed HSEFs is not directly affected by the selection. Since the HSEF occurrence during periods without burst-mode sampling is unknown, the burst-mode selection bias cannot be fully assessed, and unbiased campaigns in the overall magnetotail are needed to evaluate the effect of SITL selection on the HSEF occurrence. The dawn-dusk asymmetry is consistent with the spatial properties of reconnection-related processes and structures, including BBFs (Lotko et al., 2014; Nagai et al., 2013), magnetic reconnection (Nagai et al., 2023), current sheets (Rong et al., 2011), IDRs (Lu et al., 2018; Rogers et al., 2023), flux ropes (Imber et al., 2011), and DFs (Liu et al., 2013; Xiao et al., 2017), implying that HSEFs may be closely associated with magnetic reconnection. Additionally, Z. Zhang et al. (2024) found that the thin current sheets in the Earth's magnetotail are almost dawn-dusk symmetry, while the dusk-side current sheets are thinner and exhibit stronger current intensity. Therefore, as the main current carriers, electrons may have higher velocities on the dusk side. This suggests that relaxing the speed threshold of the HSEFs may modify the dawn-dusk asymmetry.

The high-speed electron flows are widely observed in different plasma environments, including PS, PSBL, and lobe regions. In the PS, the tailward moving HSEF events are almost symmetrically to the earthward moving events. Within the 27 events near the neutral line, 24 events exhibit similar characteristics with the super-Alfvénic electron outflow generated by the magnetic reconnection (Ergun et al., 2018; W. Y. Li et al., 2021; Tang et al., 2022; Torbert et al., 2018; Zhou et al., 2019), including the same signs of V_{eX} and V_{iX}, large V_{eY} components, and isotropic eVDFs $\left(T_{e\parallel} \sim T_{e\perp}\right)$. Away from the neutral line, those HSEF events mainly move along the local magnetic field and exhibit strong $T_{e\parallel} > T_{e\perp}$ features, while the rest HSEF events with quasi-perpendicular anisotropy are probably located in the separatrix layers. We find some HSEFs in the plasma sheet, which are embedded into an ion flow reversal and accompanied by transient electron bulk speed reversal, indicating those HSEFs may be related to the electron watersheds (Motoba et al., 2022; Sitnov et al., 2021). In the PSBL and lobe regions, the HSEF events predominantly move along the local magnetic field. The large bulk speeds come from fast bulk motion of a single electron population (usually with bi-directional feature) or a combination of an extremely fast electron beam with a nearly stagnant background population, and exhibit $T_{e\parallel}/T_{e\perp} > 1$ for most cases. 70% of the HSEFs in the PSBL have opposite V_{eX} signs with V_{iX}, indicating inflowing electron features. Though only 24 HSEF events are observed in ion flows with $|V_{iX}| > 200$ km/s, and 20 of them move toward the X-line, consistent with the inflowing electron features. As an example shown in Figure 6, the HSEFs observed in lobe regions could locate near the reconnection electron edges. In the PSBL and lobe regions, only several HSEF events are observed in Regime TT due to the apogee of MMS. However, the HSEF events in

Regime TT are nearly symmetry with in Regime EE in the PS. Those events move along the same direction with ion flows, indicating the strong correlation with magnetic reconnection. In magnetic reconnection, the electron-scale dynamic processes are local, so the distribution on both sides of the X-line is almost symmetric.

The magnetotail high-speed electron flows are found to be associated with magnetic reconnection, and HSEFs with different features are widely distributed in different regions of reconnection. Those statistical results using high-resolution MMS data reveal fundamental properties of HSEF in collisionless plasma environment. Their complex electron-kinetic features and their close relation with reconnection deepen the understanding of the electron physics throughout the Earth's magnetosphere, radio bursts associated with solar (Chen et al., 2014) and stellar eruptions (B. Zhang, 2023), and plasma wave emissions in the giant magnetospheres (Gurnett et al., 2005).

Conflict of Interest

The authors declare no conflicts of interest relevant to this study.

Data Availability Statement

The MMS data are obtained from the MMS Science Data Center (https://lasp.colorado.edu/mms/sdc/public/about/browse-wrapper/). The IRFU-Matlab package used to analyze the data in this study can be downloaded from Y. Khotyaintsev et al. (2024). The HSEF event list in this study can be accessed from Liu et al. (2025).

Acknowledgments

This work was supported by the National Key R&D Program of China (2021YFA0718600), NNSFC Grants 42188101, 42274211, 41974170, 42122032, and 41974196, Chinese Academy of Sciences (QYZDJSSW-JSC028, XDA15052500, XDA17010301, and XDB41000000), CNSA D050103, Specialized Research Fund for State Key Laboratories of China, and Specialized Research Fund for Laboratory of Geospace Environment of USTC. CN acknowledges support from the Research Council of Norway under Contract No. 300865, and the Swedish National Space Agency (SNSA) under Grant 2022-00121.

References

Angelopoulos, V., Baumjohann, W., Kennel, C. F., Coroniti, F. V., Kivelson, M. G., Pellat, R., et al. (1992). Bursty bulk flows in the inner central plasma sheet. *Journal of Geophysical Research*, *97*(A4), 4027–4039. https://doi.org/10.1029/91ja02701

Angelopoulos, V., McFadden, J. P., Larson, D., Carlson, C. W., Mende, S. B., Frey, H., et al. (2008). Tail reconnection triggering substorm onset. *Science*, *321*(5891), 931–935. https://doi.org/10.1126/science.1160495

Angelopoulos, V., Phan, T. D., Larson, D. E., Mozer, F. S., Lin, R. P., Tsuruda, K., et al. (1997). Magnetotail flow bursts: Association to global magnetospheric circulation, relationship to ionospheric activity and direct evidence for localization. *Geophysical Research Letters*, *24*(18), 2271–2274. https://doi.org/10.1029/97gl02355

Argall, M. R., Small, C. R., Piatt, S., Breen, L., Petrik, M., Kokkonen, K., et al. (2020). Mms sitl ground loop: Automating the burst data selection process. *Frontiers in Astronomy and Space Sciences*, *7*, 54. https://doi.org/10.3389/fspas.2020.00054

Baker, D. N., Pulkkinen, T., Angelopoulos, V., Baumjohann, W., & McPherron, R. (1996). Neutral line model of substorms: Past results and present view. *Journal of Geophysical Research*, *101*(A6), 12975–13010. https://doi.org/10.1029/95JA03753

Baumjohann, W., Hesse, M., Kokubun, S., Mukai, T., Nagai, T., & Petrukovich, A. (1999). Substorm dipolarization and recovery. *Journal of Geophysical Research*, *104*(A11), 24995–25000. https://doi.org/10.1029/1999JA900282

Baumjohann, W., Paschmann, G., & Cattell, C. A. (1989). Average plasma properties in the central plasma sheet. *Journal of Geophysical Research*, *94*(A6), 6597–6606. https://doi.org/10.1029/JA094iA06p06597

Birn, J., Hesse, M., Runov, A., & Zhou, X.-Z. (2015). Ion beams in the plasma sheet boundary layer. *Journal of Geophysical Research: Space Physics*, *120*(9), 7522–7535. https://doi.org/10.1002/2015JA021573

Blake, J. B., Mauk, B. H., Baker, D. N., Carranza, P., Clemmons, J. H., Craft, J., et al. (2016). The fly's eye energetic particle spectrometer (FEEPS) sensors for the magnetospheric multiscale (MMS) mission. *Space Science Reviews*, *199*(1–4), 309–329. https://doi.org/10.1007/s11214-015-0163-x

Boakes, P. D., Nakamura, R., Volwerk, M., & Milan, S. E. (2014). Eclat cluster spacecraft magnetotail plasma region identifications (2001–2009). *Dataset Papers in Science*, *2014*, 1–13. https://doi.org/10.1155/2014/684305

Burch, J. L., Moore, T. E., Torbert, R. B., & Giles, B. L. (2016a). Magnetospheric multiscale overview and science objectives. *Space Science Reviews*, *199*(1–4), 5–21. https://doi.org/10.1007/s11214-015-0164-9

Burch, J. L., Torbert, R. B., Phan, T. D., Chen, L. J., Moore, T. E., Ergun, R. E., et al. (2016b). Electron-scale measurements of magnetic reconnection in space. *Science*, *352*(6290), aaf2939. https://doi.org/10.1126/science.aaf2939

Cao, J. B., Ma, Y. D., Parks, G., Reme, H., Dandouras, I., Nakamura, R., et al. (2006). Joint observations by cluster satellites of bursty bulk flows in the magnetotail. *Journal of Geophysical Research*, *111*(A4), A04206. https://doi.org/10.1029/2005ja011322

Cattell, C., Dombeck, J., Wygant, J., Drake, J. F., Swisdak, M., Goldstein, M. L., et al. (2005). Cluster observations of electron holes in association with magnetotail reconnection and comparison to simulations. *Journal of Geophysical Research*, *110*(A1), A01211. https://doi.org/10.1029/2004ja010519

Chappell, C. R., Giles, B. L., Moore, T. E., Delcourt, D. C., Craven, P. D., & Chandler, M. O. (2000). The adequacy of the ionospheric source in supplying magnetospheric plasma. *Journal of Atmospheric and Solar-Terrestrial Physics*, *62*(6), 421–436. https://doi.org/10.1016/S1364-6826(00)00021-3

Chappell, C. R., Moore, T. E., & Waite, J. H. (1987). The ionosphere as a fully adequate source of plasma for the Earth's magnetosphere. *Journal of Geophysical Research*, *92*(A6), 5896–5910. https://doi.org/10.1029/JA092iA06p05896

Chen, C. X., & Wolf, R. A. (1993). Interpretation of high-speed flows in the plasma sheet. *Journal of Geophysical Research*, *98*(A12), 21409–21419. https://doi.org/10.1029/93ja02080

Chen, L. J., Bessho, N., Lefebvre, B., Vaith, H., Fazakerley, A., Bhattacharjee, A., et al. (2008). Evidence of an extended electron current sheet and its neighboring magnetic island during magnetotail reconnection. *Journal of Geophysical Research*, *113*(A12), A12213. https://doi.org/10.1029/2008ja013385

Chen, L. J., Wang, S., Hesse, M., Ergun, R. E., Moore, T., Giles, B., et al. (2019). Electron diffusion regions in magnetotail reconnection under varying guide fields. *Geophysical Research Letters*, *46*(12), 6230–6238. https://doi.org/10.1029/2019gl082393

Chen, Y., Du, G., Feng, L., Feng, S., Kong, X., Guo, F., et al. (2014). A solar type II radio burst from coronal mass ejection-coronal ray interaction: Simultaneous radio and extreme ultraviolet imaging. *The Astrophysical Journal*, *787*(1), 59. https://doi.org/10.1088/0004-637X/787/1/59

Drake, J. F., Swisdak, M., Cattell, C., Shay, M. A., Rogers, B. N., & Zeiler, A. (2003). Formation of electron holes and particle energization during magnetic reconnection. *Science*, *299*(5608), 873–877. https://doi.org/10.1126/science.1080333

Eastman, T. E., Frank, L. A., Peterson, W. K., & Lennartsson, W. (1984). The plasma sheet boundary layer. *Journal of Geophysical Research*, *89*(A3), 1553–1572. https://doi.org/10.1029/JA089iA03p01553

Eastwood, J. P., Phan, T. D., Øieroset, M., Shay, M. A., Malakit, K., Swisdak, M., et al. (2013). Influence of asymmetries and guide fields on the magnetic reconnection diffusion region in collisionless space plasmas. *Plasma Physics and Controlled Fusion*, *55*(12), 124001. https://doi.org/10.1088/0741-3335/55/12/124001

Egedal, J., Daughton, W., & Le, A. (2012). Large-scale electron acceleration by parallel electric fields during magnetic reconnection. *Nature Physics*, *8*(4), 321–324. https://doi.org/10.1038/nphys2249

Egedal, J., Daughton, W., Le, A., & Borg, A. L. (2015). Double layer electric fields aiding the production of energetic flat-top distributions and superthermal electrons within magnetic reconnection exhausts. *Physics of Plasmas*, *22*(10), 101208. https://doi.org/10.1063/1.4933055

Egedal, J., Le, A., & Daughton, W. (2013). A review of pressure anisotropy caused by electron trapping in collisionless plasma, and its implications for magnetic reconnection. *Physics of Plasmas*, *20*(6), 061201. https://doi.org/10.1063/1.4811092

Egedal, J., Ng, J., Le, A., Daughton, W., Wetherton, B., Dorelli, J., et al. (2019). Pressure tensor elements breaking the frozen-in law during reconnection in Earth's magnetotail. *Physical Review Letters*, *123*(22), 225101. https://doi.org/10.1103/PhysRevLett.123.225101

Ergun, R. E., Ahmadi, N., Kromyda, L., Schwartz, S. J., Chasapis, A., Hoilijoki, S., et al. (2020b). Particle acceleration in strong turbulence in the Earth's magnetotail. *The Astrophysical Journal*, *898*(2), 15. https://doi.org/10.3847/1538-4357/ab9ab5

Ergun, R. E., Ahmadi, N., Kromyda, L., Schwartz, S. J., Chasapis, A., Hoilijoki, S., et al. (2020a). Observations of particle acceleration in magnetic reconnection–driven turbulence. *The Astrophysical Journal*, *898*(2), 13. https://doi.org/10.3847/1538-4357/ab9ab6

Ergun, R. E., Goodrich, K. A., Wilder, F. D., Ahmadi, N., Holmes, J. C., Eriksson, S., et al. (2018). Magnetic reconnection, turbulence, and particle acceleration: Observations in the Earth's magnetotail. *Geophysical Research Letters*, *45*(8), 3338–3347. https://doi.org/10.1002/2018gl076993

Ergun, R. E., Tucker, S., Westfall, J., Goodrich, K. A., Malaspina, D. M., Summers, D., et al. (2016). The axial double probe and fields signal processing for the mms mission. *Space Science Reviews*, *199*(1–4), 167–188. https://doi.org/10.1007/s11214-014-0115-x

Frank, L. A. (1985). Plasmas in the Earth's magnetotail. *Space Science Reviews*, *42*(1–2), 211–240. https://doi.org/10.1007/BF00218233

Fu, X. R., Lu, Q. M., & Wang, S. (2006). The process of electron acceleration during collisionless magnetic reconnection. *Physics of Plasmas*, *13*(1), 012309. https://doi.org/10.1063/1.2164808

Gershman, D. J., Avanov, L. A., Boardsen, S. A., Dorelli, J. C., Gliese, U., Barrie, A. C., et al. (2017). Spacecraft and instrument photoelectrons measured by the dual electron spectrometers on MMS. *Journal of Geophysical Research: Space Physics*, *122*(11), 11548–11558. https://doi.org/10.1002/2017ja024518

Gershman, D. J., Dorelli, J. C., Avanov, L. A., Gliese, U., Barrie, A., Schiff, C., et al. (2019). Systematic uncertainties in plasma parameters reported by the fast plasma investigation on nasa's magnetospheric multiscale mission. *Journal of Geophysical Research: Space Physics*, *124*(12), 10345–10359. https://doi.org/10.1029/2019ja026980

Gosling, J. T., Baker, D. N., Bame, S. J., Feldman, W. C., Zwickl, R. D., & Smith, E. J. (1985). North-south and dawn-dusk plasma asymmetries in the distant tail lobes: Isee 3. *Journal of Geophysical Research*, *90*(A7), 6354–6360. https://doi.org/10.1029/JA090iA07p06354

Graham, D. B., Khotyaintsev, Y. V., & André, M. (2023). Langmuir and upper hybrid waves in Earth's magnetotail. *Journal of Geophysical Research: Space Physics*, *128*(10), e2023JA031900. https://doi.org/10.1029/2023ja031900

Graham, D. B., Khotyaintsev, Y. V., Norgren, C., Vaivads, A., André, M., Drake, J. F., et al. (2019). Universality of lower hybrid waves at Earth's magnetopause. *Journal of Geophysical Research: Space Physics*, *124*(11), 8727–8760. https://doi.org/10.1029/2019ja027155

Grigorenko, E. E., Koleva, R., & Sauvaud, J. A. (2012). On the problem of plasma sheet boundary layer identification from plasma moments in Earth's magnetotail. *Annales Geophysicae*, *30*(9), 1331–1343. https://doi.org/10.5194/angeo-30-1331-2012

Gurnett, D. A., Kurth, W. S., Hospodarsky, G. B., Persoon, A. M., Averkamp, T. F., Cecconi, B., et al. (2005). Radio and plasma wave observations at saturn from Cassini's approach and first orbit. *Science*, *307*(5713), 1255–1259. https://doi.org/10.1126/science.1105356

Haaland, S., Lybekk, B., Maes, L., Laundal, K., Pedersen, A., Tenfjord, P., et al. (2017). North-south asymmetries in cold plasma density in the magnetotail lobes: Cluster observations. *Journal of Geophysical Research: Space Physics*, *122*(1), 136–149. https://doi.org/10.1002/2016ja023404

Haaland, S., Paschmann, G., Förster, M., Quinn, J., Torbert, R., Vaith, H., et al. (2008). Plasma convection in the magnetotail lobes: Statistical results from cluster EDI measurements. *Annales Geophysicae*, *26*(8), 2371–2382. https://doi.org/10.5194/angeo-26-2371-2008

Hoshino, M., Mukai, T., Terasawa, T., & Shinohara, I. (2001). Suprathermal electron acceleration in magnetic reconnection. *Journal of Geophysical Research*, *106*(A11), 25979–25997. https://doi.org/10.1029/2001ja900052

Huang, C., Lu, Q., & Wang, S. (2010). The mechanisms of electron acceleration in antiparallel and guide field magnetic reconnection. *Physics of Plasmas*, *17*(7), 072306. https://doi.org/10.1063/1.3457930

Huang, S. Y., Wei, Y. Y., Yuan, Z. G., Jiang, K., Deng, X. H., Xu, S. B., et al. (2020). Electron jets in the terrestrial magnetotail: A statistical overview. *The Astrophysical Journal*, *896*(1), 8. https://doi.org/10.3847/1538-4357/ab8eb0

Hubbert, M., Russell, C. T., Qi, Y., Lu, S., Burch, J. L., Giles, B. L., & Moore, T. E. (2022). Electron-only reconnection as a transition phase from quiet magnetotail current sheets to traditional magnetotail reconnection. *Journal of Geophysical Research: Space Physics*, *127*(3), 28. https://doi.org/10.1029/2021ja029584

Imada, S., Nakamura, R., Daly, P. W., Hoshino, M., Baumjohann, W., Mühlbachler, S., et al. (2007). Energetic electron acceleration in the downstream reconnection outflow region. *Journal of Geophysical Research*, *112*(A3), A03202. https://doi.org/10.1029/2006ja011847

Imber, S. M., Slavin, J. A., Auster, H. U., & Angelopoulos, V. (2011). A themis survey of flux ropes and traveling compression regions: Location of the near-earth reconnection site during solar minimum. *Journal of Geophysical Research*, *116*(A2), A02201. https://doi.org/10.1029/2010ja016026

Kaufmann, R. L., Paterson, W. R., & Frank, L. A. (2005). Relationships between the ion flow speed, magnetic flux transport rate, and other plasma sheet parameters. *Journal of Geophysical Research*, *110*(A9), A09216. https://doi.org/10.1029/2005ja011068

Khotyaintsev, Y., Nilsson, T., Johansson, E. P. G., Vaivads, A., Graham, D., Karlsson, J., et al. (2024). Irfu-matlab (v1.17.0) [Software]. *Zenodo*. https://doi.org/10.5281/zenodo.14525047

Khotyaintsev, Y. V., Graham, D. B., Norgren, C., Eriksson, E., Li, W., Johlander, A., et al. (2016). Electron jet of asymmetric reconnection. *Geophysical Research Letters*, *43*(11), 5571–5580. https://doi.org/10.1002/2016gl069064

Kim, H.-S., Lee, D.-Y., Ohtani, S.-I., Lee, E.-S., & Ahn, B.-H. (2010). Some statistical properties of flow bursts in the magnetotail. *Journal of Geophysical Research*, *115*(A12), A12229. https://doi.org/10.1029/2009ja015173

Lazarian, A., & Opher, M. (2009). A model of acceleration of anomalous cosmic rays by reconnection in the heliosheath. *The Astrophysical Journal*, *703*(1), 8–21. https://doi.org/10.1088/0004-637X/703/1/8

Li, W. Y., Graham, D. B., Khotyaintsev, Y. V., Vaivads, A., André, M., Min, K., et al. (2020). Electron bernstein waves driven by electron crescents near the electron diffusion region. *Nature Communications*, *11*(1), 141. https://doi.org/10.1038/s41467-019-13920-w

Li, W. Y., Khotyaintsev, Y. V., Tang, B. B., Graham, D. B., Norgren, C., Vaivads, A., et al. (2021). Upper-hybrid waves driven by meandering electrons around magnetic reconnection x line. *Geophysical Research Letters*, *48*(16), 9. https://doi.org/10.1029/2021gl093164

Li, X., Wang, R., & Lu, Q. (2023). Division of magnetic flux rope via magnetic reconnection observed in the magnetotail. *Geophysical Research Letters*, *50*(1), e2022GL101084. https://doi.org/10.1029/2022gl101084

Lin, R. P., & Hudson, H. S. (1971). 10 100 kev electron acceleration and emission from solar flares. *Solar Physics*, *17*(2), 412–435. https://doi.org/10.1007/BF00150045

Lin, R. P., Krucker, S., Hurford, G. J., Smith, D. M., Hudson, H. S., Holman, G. D., et al. (2003). Rhessi observations of particle acceleration and energy release in an intense solar gamma-ray line flare. *The Astrophysical Journal*, *595*(2), L69–L76. https://doi.org/10.1086/378932

Lindqvist, P. A., Olsson, G., Torbert, R. B., King, B., Granoff, M., Rau, D., et al. (2016). The spin-plane double probe electric field instrument for mms. *Space Science Reviews*, *199*(1–4), 137–165. https://doi.org/10.1007/s11214-014-0116-9

Lindstedt, T., Khotyaintsev, Y. V., Vaivads, A., André, M., Fear, R. C., Lavraud, B., et al. (2009). Separatrix regions of magnetic reconnection at the magnetopause. *Annales Geophysicae*, *27*(10), 4039–4056. https://doi.org/10.5194/angeo-27-4039-2009

Liu, H., Li, W., Tang, B., Norgren, C., Liu, K., Khotyaintsev, Y., et al. (2025). High-speed electron flows in the Earth magnetotail [Dataset]. *Zenodo*. https://doi.org/10.5281/zenodo.14842767

Liu, J., Angelopoulos, V., Runov, A., & Zhou, X. Z. (2013). On the current sheets surrounding dipolarizing flux bundles in the magnetotail: The case for wedgelets. *Journal of Geophysical Research: Space Physics*, *118*(5), 2000–2020. https://doi.org/10.1002/jgra.50092

Lotko, W., Smith, R. H., Zhang, B., Ouellette, J. E., Brambles, O. J., & Lyon, J. G. (2014). Space weather. ionospheric control of magnetotail reconnection. *Science*, *345*(6193), 184–187. https://doi.org/10.1126/science.1252907

Lu, Q., Huang, C., Xie, J., Wang, R., Wu, M., Vaivads, A., & Wang, S. (2010). Features of separatrix regions in magnetic reconnection: Comparison of 2-d particle-in-cell simulations and cluster observations. *Journal of Geophysical Research*, *115*(A11), A11208. https://doi.org/10.1029/2010ja015713

Lu, S., Lin, Y., Angelopoulos, V., Artemyev, A. V., Pritchett, P. L., Lu, Q., & Wang, X. Y. (2016). Hall effect control of magnetotail dawn-dusk asymmetry: A three-dimensional global hybrid simulation. *Journal of Geophysical Research: Space Physics*, *121*(12), 11882–11895. https://doi.org/10.1002/2016ja023325

Lu, S., Pritchett, P. L., Angelopoulos, V., & Artemyev, A. V. (2018). Formation of dawn-dusk asymmetry in Earth's magnetotail thin current sheet: A three-dimensional particle-in-cell simulation. *Journal of Geophysical Research: Space Physics*, *123*(4), 2801–2814. https://doi.org/10.1002/2017JA025095

Ma, W., Zhou, M., Zhong, Z., & Deng, X. (2022). Contrasting the mechanisms of reconnection-driven electron acceleration with in situ observations from MMS in the terrestrial magnetotail. *The Astrophysical Journal*, *931*(2), 135. https://doi.org/10.3847/1538-4357/ac6be6

Ma, Y. D., Cao, J. B., Nakamura, R., Zhang, T. L., Reme, H., Dandouras, I., et al. (2009). Statistical analysis of earthward flow bursts in the inner plasma sheet during substorms. *Journal of Geophysical Research*, *114*(A7), A07215. https://doi.org/10.1029/2009JA014275

Man, H., Zhou, M., Zhong, Z., Deng, X., & Li, H. (2021). Statistics of the intense current structure in the dayside magnetopause boundary layer. *Essoar*, *126*(12), e29890. https://doi.org/10.1002/essoar.10506792.1

Marshall, A. T., Burch, J. L., Reiff, P. H., Webster, J. M., Torbert, R. B., Ergun, R. E., et al. (2020). Asymmetric reconnection within a flux rope-type dipolarization front. *Journal of Geophysical Research: Space Physics*, *125*(1), e27296. https://doi.org/10.1029/2019ja027296

Matsumoto, H., Kojima, H., Miyatake, T., Omura, Y., Okada, M., Nagano, I., & Tsutsui, M. (1994). Electrostatic solitary waves (ESW) in the magnetotail: Ben wave forms observed by geotail. *Geophysical Research Letters*, *21*(25), 2915–2918. https://doi.org/10.1029/94gl01284

Mauk, B. H., Blake, J. B., Baker, D. N., Clemmons, J. H., Reeves, G. D., Spence, H. E., et al. (2016). The energetic particle detector (EPD) investigation and the energetic ion spectrometer (EIS) for the magnetospheric multiscale (MMS) mission. *Space Science Reviews*, *199*(1–4), 471–514. https://doi.org/10.1007/s11214-014-0055-5

Milan, S. E., Clausen, L. B. N., Coxon, J. C., Carter, J. A., Walach, M. T., Laundal, K., et al. (2017). Overview of solar wind-magnetosphere-ionosphere-atmosphere coupling and the generation of magnetospheric currents. *Space Science Reviews*, *206*(1–4), 547–573. https://doi.org/10.1007/s11214-017-0333-0

Motoba, T., Sitnov, M. I., Stephens, G. K., & Gershman, D. J. (2022). A new perspective on magnetotail electron and ion divergent flows: MMS observations. *Journal of Geophysical Research (Space Physics)*, *127*(10), e2022JA030514. https://doi.org/10.1029/2022JA030514

Nagai, T., Fujimoto, M., Saito, Y., Machida, S., Terasawa, T., Nakamura, R., et al. (1998). Structure and dynamics of magnetic reconnection for substorm onsets with Geotail observations. *Journal of Geophysical Research*, *103*(A3), 4419–4440. https://doi.org/10.1029/97JA02190

Nagai, T., Shinohara, I., Saito, Y., Ieda, A., & Nakamura, R. (2023). Location and timing of magnetic reconnections in Earth's magnetotail: Accomplishments of the 29-year geotail near-earth magnetotail survey. *Journal of Geophysical Research: Space Physics*, *128*(12), e2023JA032023. https://doi.org/10.1029/2023JA032023

Nagai, T., Shinohara, I., Zenitani, S., Nakamura, R., Nakamura, T. K. M., Fujimoto, M., et al. (2013). Three-dimensional structure of magnetic reconnection in the magnetotail from Geotail observations. *Journal of Geophysical Research: Space Physics*, *118*(4), 1667–1678. https://doi.org/10.1002/jgra.50247

Nakai, H., Kamide, Y., & Russell, C. T. (1991). Influences of solar wind parameters and geomagnetic activity on the tail lobe magnetic field: A statistical study. *Journal of Geophysical Research*, *96*(A4), 5511–5523. https://doi.org/10.1029/90JA02361

Nakamura, R., Baumjohann, W., Runov, A., Volwerk, M., Zhang, T. L., Klecker, B., et al. (2002). Fast flow during current sheet thinning. *Geophysical Research Letters*, *29*(23), 2140. https://doi.org/10.1029/2002GL016200

Norgren, C., Hesse, M., Graham, D. B., Khotyaintsev, Y. V., Tenfjord, P., Vaivads, A., et al. (2020). Electron acceleration and thermalization at magnetotail separatrices. *Journal of Geophysical Research: Space Physics*, *125*(4), e27440. https://doi.org/10.1029/2019ja027440

Ohtani, S., Kokubun, S., Elphic, R. C., & Russell, C. T. (1988). Field-aligned current signatures in the near-tail region: 1. Isee observations in the plasma sheet boundary layer. *Journal of Geophysical Research*, *93*(A9), 9709–9720. https://doi.org/10.1029/JA093iA09p09709

Oieroset, M., Phan, T. D., Fujimoto, M., Lin, R. P., & Lepping, R. P. (2001). In situ detection of collisionless reconnection in the Earth's magnetotail. *Nature*, *412*(6845), 414–417. https://doi.org/10.1038/35086520

Onsager, T., Thomsen, M., Elphic, R., & Gosling, J. (1991). Model of electron and ion distributions in the plasma sheet boundary layer. *Journal of Geophysical Research*, *96*(A12), 20999–21011. https://doi.org/10.1029/91JA01983

Paschmann, G., & Daly, P. W. (1998). *Analysis methods for multi-spacecraft data* (Vol. 1). ISSI Scientific Reports Series SR-001, ESA/ISSI.

Phan, T. D., Eastwood, J. P., Cassak, P. A., Øieroset, M., Gosling, J. T., Gershman, D. J., et al. (2016). Mms observations of electron-scale filamentary currents in the reconnection exhaust and near the x line. *Geophysical Research Letters*, *43*(12), 6060–6069. https://doi.org/10.1002/2016gl069212

Pollock, C., Moore, T., Jacques, A., Burch, J., Gliese, U., Saito, Y., et al. (2016). Fast plasma investigation for magnetospheric multiscale. *Space Science Reviews*, *199*(1–4), 331–406. https://doi.org/10.1007/s11214-016-0245-4

Pritchett, P. L. (2008). Energetic electron acceleration during multi-island coalescence. *Physics of Plasmas*, *15*(10), 102105. https://doi.org/10.1063/1.2996321

Qi, Y., Ergun, R., Pathak, N., Phan, T. D., Burch, J. L., Chasapis, A., et al. (2024). Investigation of a magnetic reconnection event with extraordinarily high particle energization in magnetotail turbulence. *The Astrophysical Journal Letters*, *962*(2), L39. https://doi.org/10.3847/2041-8213/ad24eb

Raj, A., Phan, T., Lin, R. P., & Angelopoulos, V. (2002). Wind survey of high-speed bulk flows and field-aligned beams in the near-earth plasma sheet. *Journal of Geophysical Research*, *107*(A12), 1419. https://doi.org/10.1029/2001ja007547

Rogers, A. J., Farrugia, C. J., Torbert, R. B., & Rogers, T. J. (2023). Applying magnetic curvature to mms data to identify thin current sheets relative to tail reconnection. *Journal of Geophysical Research: Space Physics*, *128*(1), e2022JA030577. https://doi.org/10.1029/2022ja030577

Rong, Z. J., Wan, W. X., Shen, C., Li, X., Dunlop, M. W., Petrukovich, A. A., et al. (2011). Statistical survey on the magnetic structure in magnetotail current sheets. *Journal of Geophysical Research*, *116*(A9), A09218. https://doi.org/10.1029/2011ja016489

Russell, C. T., Anderson, B. J., Baumjohann, W., Bromund, K. R., Dearborn, D., Fischer, D., et al. (2016). The magnetospheric multiscale magnetometers. *Space Science Reviews*, *199*(1–4), 189–256. https://doi.org/10.1007/s11214-014-0057-3

Shay, M. A., Drake, J. F., Swisdak, M., Dorland, W., & Rogers, B. N. (2003). Inherently three dimensional magnetic reconnection: A mechanism for bursty bulk flows? *Geophysical Research Letters*, *30*(6), 1345. https://doi.org/10.1029/2002gl016267

Shi, Q. Q., Zong, Q. G., Fu, S. Y., Dunlop, M. W., Pu, Z. Y., Parks, G. K., et al. (2013). Solar wind entry into the high-latitude terrestrial magnetosphere during geomagnetically quiet times. *Nature Communications*, *4*(1), 1466. https://doi.org/10.1038/ncomms2476

Shue, J. H., Song, P., Russell, C. T., Steinberg, J. T., Chao, J. K., Zastenker, G., et al. (1998). Magnetopause location under extreme solar wind conditions. *Journal of Geophysical Research*, *103*(A8), 17691–17700. https://doi.org/10.1029/98ja01103

Shukhtina, M. A., Dmitrieva, N. P., & Sergeev, V. A. (2004). Quantitative magnetotail characteristics of different magnetospheric states. *Annales Geophysicae*, *22*(3), 1019–1032. https://doi.org/10.5194/angeo-22-1019-2004

Sitnov, M. I., Motoba, T., & Swisdak, M. (2021). Multiscale nature of the magnetotail reconnection onset. *Geophysical Research Letters*, *48*(10), e93065. https://doi.org/10.1029/2021GL093065

Svenes, K. R., Lybekk, B., Pedersen, A., & Haaland, S. (2008). Cluster observations of near-earth magnetospheric lobe plasma densities – A statistical study. *Annales Geophysicae*, *26*(9), 2845–2852. https://doi.org/10.5194/angeo-26-2845-2008

Tang, B. B., Li, W. Y., Khotyaintsev, Y. V., Graham, D. B., Gao, C. H., Chen, Z. Z., et al. (2022). Fine structures of the electron current sheet in magnetotail guide-field reconnection. *Geophysical Research Letters*, *49*(9), e97573. https://doi.org/10.1029/2021gl097573

Torbert, R. B., Burch, J. L., Phan, T. D., Hesse, M., Argall, M. R., Shuster, J., et al. (2018). Electron-scale dynamics of the diffusion region during symmetric magnetic reconnection in space. *Science*, *362*(6421), 1391–1395. https://doi.org/10.1126/science.aat2998

Tsyganenko, N. A. (2000). Solar wind control of the tail lobe magnetic field as deduced from geotail, ampte/irm, and isee 2 data. *Journal of Geophysical Research*, *105*(A3), 5517–5528. https://doi.org/10.1029/1999ja000375

Vo, T., Ergun, R. E., Usanova, M. E., & Chasapis, A. (2023). Mesoscale structure and properties of the terrestrial magnetotail plasma sheet from the magnetospheric multiscale mission. *Journal of Geophysical Research: Space Physics*, *128*(9), e2023JA031358. https://doi.org/10.1029/2023ja031358

Wang, H.-W., Tang, B.-B., Li, W., Zhang, Y.-C., Graham, D. B., Khotyaintsev, Y. V., et al. (2023). Electron dynamics in the electron current sheet during strong guide-field reconnection. *Geophysical Research Letters*, *50*(10), e2023GL103046. https://doi.org/10.1029/2023GL103046

Wang, L., Huang, C., Du, A., & Ge, Y. (2022a). Hall nature ahead of dipolarization fronts in the Earth's magnetotail: A statistical study for MMS data. *Geophysical Research Letters*, *49*(3), e97075. https://doi.org/10.1029/2021GL097075

Wang, R., Lu, Q., Huang, C., & Wang, S. (2010). Multispacecraft observation of electron pitch angle distributions in magnetotail reconnection. *Journal of Geophysical Research*, *115*(A1), A01209. https://doi.org/10.1029/2009ja014553

Wang, S., Chen, L., Bessho, N., Ng, J., Hesse, M., Graham, D. B., et al. (2022b). Lower-hybrid wave structures and interactions with electrons observed in magnetotail reconnection diffusion regions. *Journal of Geophysical Research: Space Physics*, *127*(5), e30109. https://doi.org/10.1029/2021ja030109

Webster, J. M., Burch, J. L., Reiff, P. H., Daou, A. G., Genestreti, K. J., Graham, D. B., et al. (2018). Magnetospheric multiscale dayside reconnection electron diffusion region events. *Journal of Geophysical Research: Space Physics*, *123*(6), 4858–4878. https://doi.org/10.1029/2018ja025245

Xiao, S., Zhang, T., Wang, G., Volwerk, M., Ge, Y., Schmid, D., et al. (2017). Occurrence rate of dipolarization fronts in the plasma sheet: Cluster observations. *Annales Geophysicae*, *35*(4), 1015–1022. https://doi.org/10.5194/angeo-35-1015-2017

Young, D. T., Burch, J. L., Gomez, R. G., De Los Santos, A., Miller, G. P., Wilson, P., et al. (2016). Hot plasma composition analyzer for the magnetospheric multiscale mission. *Space Science Reviews*, *199*(1–4), 407–470. https://doi.org/10.1007/s11214-014-0119-6

Zhang, B. (2023). The physics of fast radio bursts. *Reviews of Modern Physics*, *95*(3), 035005. https://doi.org/10.1103/RevModPhys.95.035005

Zhang, Z., Lu, S., Lu, Q., Wang, R., Zhan, C., Li, X., & Artemyev, A. V. (2024). Statistical survey of thin current sheets in Earth's magnetotail: MMS observations. *Journal of Geophysical Research (Space Physics)*, *129*(5), e2024JA032575. https://doi.org/10.1029/2024JA032575

Zhou, M., Deng, X. H., Zhong, Z. H., Pang, Y., Tang, R. X., El-Alaoui, M., et al. (2019). Observations of an electron diffusion region in symmetric reconnection with weak guide field. *The Astrophysical Journal*, *870*(1), 34. https://doi.org/10.3847/1538-4357/aaf16f